Controlling periodic long-range signalling to drive a morphogenetic transition

Hugh Z Ford[1], Angelika Manhart[2] & Jonathan R Chubb[1]*

[1] Laboratory for Molecular Cell Biology and Department of Cell and Developmental Biology, University College London, United Kingdom

[2] Department of Mathematics, University College London, United Kingdom

* Corresponding author: j.chubb@ucl.ac.uk

Abstract

Cells use signal relay to transmit information across tissue scales. However, the production of information carried by signal relay remains poorly characterised. To determine how the coding features of signal relay are generated, we used the classic system for long-range signalling: the periodic cAMP waves that drive *Dictyostelium* collective migration. Combining imaging and optogenetic perturbation of cell signalling states, we find that migration is triggered by an increase in wave frequency generated at the signalling centre. Wave frequency is regulated by cAMP wave circulation, which organises the long-range signal. To determine the mechanisms modulating wave circulation, we combined mathematical modelling, the general theory of excitable media and mechanical perturbations to test competing models. Models in which cell density and spatial patterning modulate the wave frequency cannot explain the temporal evolution of signalling waves. Instead, our evidence leads to a model where wave circulation increases the ability for cell to relay the signal, causing further increase in the circulation rate. This implies that information driving a morphogenetic transition gradually unfolds due to positive feedback between cell signalling state and signalling pattern. This demonstrates how the coding properties of a long-range signal arise from self-organised wave dynamics at the signalling centre.

Introduction

Tissues require long-range signalling strategies to coordinate cell behaviour. As signal diffusion is only efficient over a few cell diameters, cells relay signals to rapidly disseminate information over tissue scales (Gelens, Anderson and Ferrell, 2014). Signals are relayed by the activation of cells in response to active neighbours, which in turn activate their own neighbours (Dieterle *et al.*, 2020). In this way, long-range signalling through tissues is propagated as waves of cell activation that travel outwardly from signalling centres (Deneke and di Talia, 2018). Prominent examples of biological activation waves include ERK waves in the developing skin, breast and colon and during wound closure (Aoki *et al.*, 2017; Ender *et al.*, 2022; Pond *et al.*, 2022), periodic activation waves in the brain (Huang *et al.*, 2010), chemoattractant waves in neutrophil swarms (Afonso *et al.*, 2012), morphogen waves during gastrulation (Liu *et al.*, 2021), waves of cell stress in bacterial biofilms (Chou *et al.*, 2022), and cAMP waves in *Dictyostelium* aggregation (Tomchik and Devreotes, 1981). Waves can also be pathological, such as in cardiac fibrillation, where waves drive muscle contraction independently of the pacemaker (Pandit and Jalife, 2013). In these examples, the behaviour of the cells is organised by a self-sustaining signalling pattern, however it is unclear how cells control the pattern to regulate the information encoded by the signal.

One of the most intensively studied paradigms for signal relay is the *Dictyostelium* transition from a single cell state to a multicellular state (Weijer, 2004). Upon starvation, single cells begin to communicate via cAMP (cyclic adenosine monophosphate) (Tomchik and Devreotes, 1981; Gregor *et al.*, 2010). Upon receipt of cAMP, cells secrete their own cAMP, which then activates the next set of cells, hence propagating the signal. As cAMP is a chemoattractant, cells move towards signalling centres, resulting in aggregation into the multicellular phase of their lifecycle. At the population level, the cAMP signal propagates in waves with circular and spiral patterns characteristic of other relay systems (Durston, 1973; Lee, Cox and Goldstein, 1996).

Despite decades of research into cAMP signalling in *Dictyostelium,* the mechanism of information production and control remain poorly characterised. Several lines of evidence suggest information is carried by cAMP wave gradient, frequency and speed and decoded by cells in terms of changes in motility (Siegert and Weijer, 1989). One view is that cells interpret an increase in the frequency of the cAMP waves as a trigger to begin collective chemotaxis (Skoge *et al.*, 2014). Alternative views are that other changing features of the waves, such as their speed and gradient, convey information instructing chemotaxis (Fisher, Merkl and Gerisch, 1989; Wessels, Murray and Soll, 1992; Song *et al.*, 2006; Nakajima *et al.*, 2014). The current paradigm explaining the changes in wave behaviour over developmental time is that cells become more excitable (i.e. more able to relay the signal) at higher cell densities, which then manifests in the changing wave dynamics coupled to the

onset of aggregation (Hofer, Sherratt and Maini, 1995; van Oss *et al.*, 1996). One caveat with this view is that it requires some degree of aggregation to initiate the signal that drives the aggregation process. This paradigm was informed by extensive theory and studies on excitable chemical systems. In these systems, changes in wave dynamics emerge from rotating spiral waves whose rotation rate and curvature specifies the frequency and speed of activation waves. The curvature and rotation rate are specified by the circulation of the signal at the signalling centre (Tyson and Keener, 1988; Winfree, 2001). However, the major limitation in uniting this theory with experiment to decipher wave generation and interpretation is that studies have looked either at macroscopic (population) or microscopic (cell) levels but not both at the same time. As a result, it is not clear how cell signalling, movement and spatial patterning at the signalling centre modulate the periodic cAMP waves that coordinate this morphogenetic transition.

To determine how population-level signalling dynamics are modulated by the signalling centre, we have leveraged a sensitive cAMP reporter to characterise collective cell signalling and motion during *Dictyostelium* aggregation, with single cell resolution, over developmental time and length scales. We find that the onset of cell aggregation coincides with an increase in wave frequency and decrease in wave speed. Optogenetic activation of cAMP signalling with defined frequencies reveals how an increase in the frequency of wave production from the signalling centre is required for efficient aggregation. These changing wave dynamics result from the increasing circulation rate of cAMP waves at the signalling centre. We show that circulation of cAMP waves spatially organises the signal as a spiral pattern, and the rotation rate and curvature of the spiral sets wave frequency and speed. We evaluate contrasting established and new hypotheses by which the circulation dynamics is regulated. We challenge the current paradigm, that increasing cell density drives an increase in cell excitability, and show that hypotheses in which wave dynamics result from cell rearrangement at the signalling centre also cannot explain the observed signalling patterns. Instead, we show that the ability for cells to relay signalling waves increases as the wave frequency increases. The creates positive feedback that gradually increases the rate of wave circulation and the ability for cells to relay the signal. Together these observations imply the dynamic behaviour of signalling driving morphogenesis results from a mutual reinforcement between cell state and signal pattern.

Results

The onset of collective cell signalling

To track the signalling state of individual cells during morphogenesis we imaged cells expressing the intensiometric cAMP signalling reporter Flamindo2 (Odaka *et al.*, 2014; Hashimura *et al.*, 2019) at an endogenous genetic locus. For simultaneous analysis of cell motion the cells also expressed a nuclear marker (H2B-mCherry) for cell tracking (Corrigan and Chubb, 2014). The fluorescence of Flamindo2 has an inverse relationship to the intracellular [cAMP]. This allows visualisation of the onset and progression of cAMP signalling wave patterns over cell populations during early development (Figure 1A and Figure 1–Video 1). To monitor the motion and signalling of individual cells in their population context, we tracked the central position of the nuclei and measured the internal [cAMP] from the mean Flamindo2 intensity of the cell body (Figure 1B, Figure 1–Supplementary Figure 1A and Figure 1–Video 2). Analysing all cell tracks simultaneously provided the means to study the onset and adaptation of signalling behaviour and collective motion of single cells in their population context (Figure 1C-1E).

Early during development, cells predominantly fired asynchronously. The proportion of spontaneously activating cells declined as the signalling behaviour became more correlated, with periodic waves of signalling including an increasing proportion of the cells (Figure 1D). Prior to the onset of cAMP waves (around 4 h after starvation), cells produced cAMP pulses spontaneously at a mean rate of around 1 pulse per 12 minutes, with a minimum of around 1 pulse per 4 minutes (Figure 1E). During this time, the population distribution of inter-activation intervals follows a gamma distribution (Figure 1E and Figure 1–Supplementary Figure 1B). We interpret this fit as there being a minimum waiting time between pulses (a refractory phase), with the exponential tail of the distribution suggesting the probability of firing is independent of the previous firing event.

The initial cAMP waves (around 4-5 hours) are broad bands of broken waves amalgamating from numerous circular patterns that expand from spontaneously activating cells (Figure 1A). Activation events prior to synchronisation are spontaneous, spatially variable and mostly do not initiate a cAMP wave. Together with the independence of successive firing events, these observations are inconsistent with the model that individual “pacemaker” cells act as the organising source of global cAMP waves. However, it may be possible that cell clusters (arising for example from random motion) may collectively act as a pacemaker (Mirollo and Strogatz, 1990; Gregor *et al.*, 2010). For example, if the cell cluster is sufficiently dense such that at least one cell in the cluster is likely to activate just after the refractory time. Nevertheless, any given cell will experience circular waves from several different sources with a variable periodicity (5-9 min).

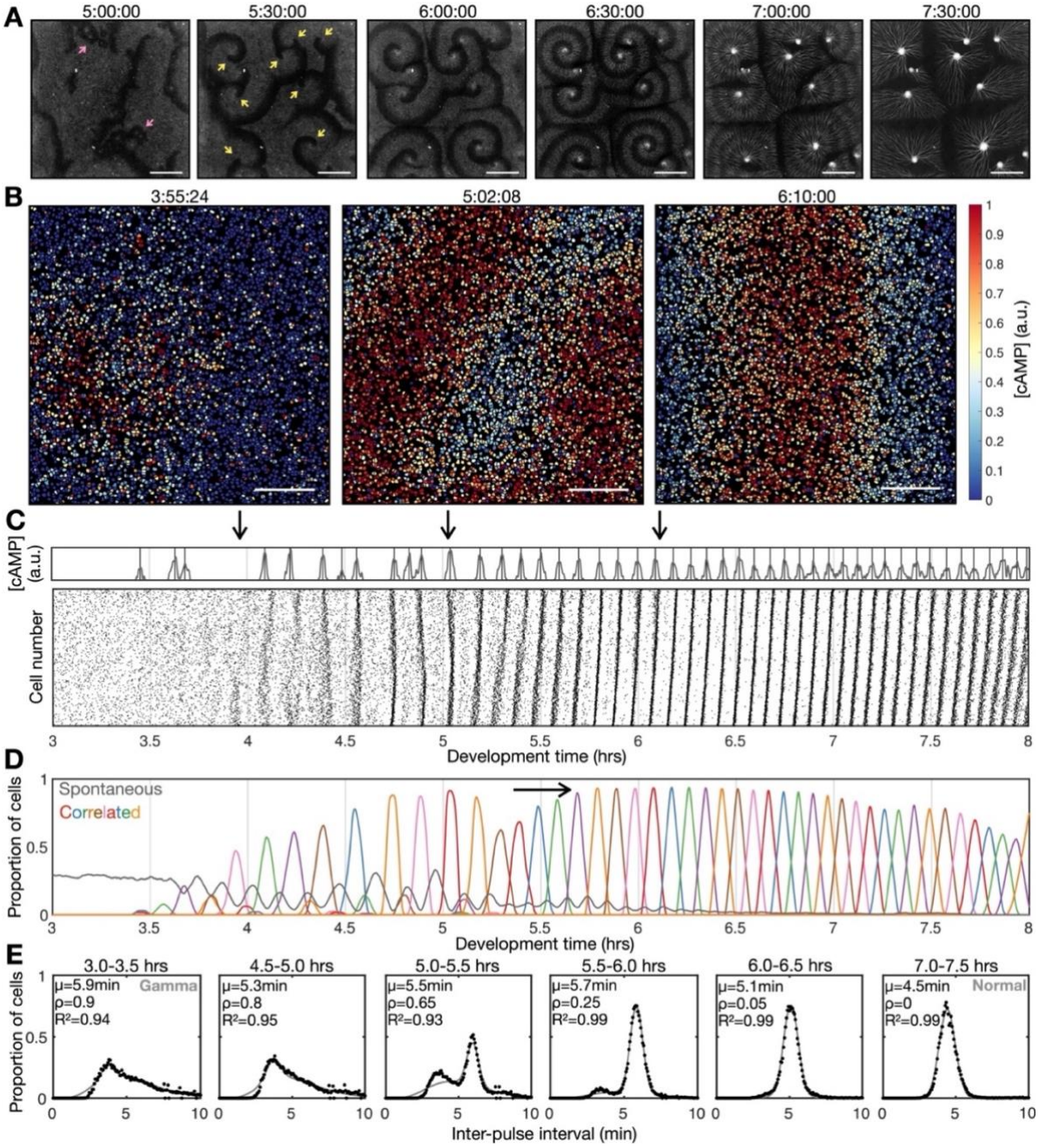

Figure 1: Transition to collective cell signalling. A) cAMP waves (dark bands) imaged using the Flamindo2 reporter following starvation. Arrows indicate circular waves (pink) and spiral waves (yellow). Scale bar: 2mm. **B)** The distribution of cells and internal [cAMP] (colour) following starvation. Scale bar: 200 µm. **C)** Representative time series of the internal [cAMP] within an individual cell (top) and a plot of signal peaks for 1000 cells (bottom). **D)** Changing proportions of correlated (coloured) and spontaneous (grey) activation events following starvation; each colour represents a single cAMP wave. Arrow: onset of spiral formation. **E)** The distribution of inter-pulse intervals over different 30 minute time intervals after starvation onset with the mean of each shown by parameter μ, together with a fitted sum of the gamma (weighted by value ρ) and normal (weighted by value 1-ρ) distribution. For the gamma distribution, the shape and rate parameter were 6.6 and 1.25 mins, the mean of the normal distribution varied (from 6 to 4.5 mins).

Circular waves produce cAMP signals at irregular intervals which are typically greater than the inter-pules interval (Figure 1D). Consequently, not all cells will relay a circular wave because cells that fire synchronously with one wave can potentially reactivate and so be refractory for the next wave. This is highlighted by a multi-peaked population distribution for inter-activation intervals where the

smallest peak is associated with spontaneous cAMP pulses while the other peaks are associated with synchronised firing during a wave (Figure 1E and Figure 1–Supplementary Figure 1B). Rotating spiral cAMP waves form from broken waves around 5-6 hours following starvation (Figure 1A). To interrogate how waves break and give rise to spiral waves, we engineered cells to express blue-photoactivable adenylyl cyclase (bPAC) (Stierl *et al.*, 2011), to control the time and place of cAMP waves by exposing a subset of cells to blue or green light (Figure 1–Supplementary Figure 2 and Figure 1–Video 3). In the absence of light pulses, we observed a steady train of periodic waves (Figure 1–Supplementary Figure 2B). Photoactivation of a small patch of cells generated a circular wave which fused with oncoming waves (Figure 1–Supplementary Figure 2A 1st and 2nd row and 2C). Wave breaks (Figure 1–Supplementary Figure 2A 4th – 6th row) occurred only when colliding with an asymmetric wave generated by the activated patch (Figure 1–Supplementary Figure 2A 3rd row). We interpret the asymmetry arising when cells activate at the border of two regions; one where cells are in a refractory state (preventing wave propagation) and the other in which cells are recovered (allowing wave propagation) (Figure 1–Supplementary Figure 2D).

Rotating spiral patterns generate waves that are more frequent and regular than circular patterns (Figure 1C-E, 5-6 hours onwards) and hence become the dominant pattern over time, overriding the less frequent circular waves, as reported in previous studies (Lee, Cox and Goldstein, 1996). The mean wave frequency steadily increased towards the maximum firing frequency of cells, around once every 3-4 minutes (Figure 1E). Consequently, the proportion of spontaneously activating cells tends to zero as there is no time to activate between waves (Figure 1D) and the population distribution of inter-pulse intervals tends to a normal distribution (Figure 1E). To understand the basis of the heterogeneity in inter-pulse intervals, we quantified the single cell differences in activation times relative to the wave centre (Figure 1–Supplementary Figure 3A,B). Aided by Markov modelling, we observed a short-term bias in firing tendencies: for example a cell that fires ahead of its neighbours has a 60% chance of repeating this early firing, 35% chance of switching to late firing and a 5% chance of skipping the subsequent wave (Figure 1–Supplementary Figure 3C,D). Whether a cell fires before or after the wave does not affect its probability of skipping a wave. Overall, these data suggest no intrinsic difference between cells beyond a slight history dependence.

The onset of collective migration

To relate how information encoded by spiral waves coordinates collective motion, we compared changes in cAMP wave dynamics to cell chemotaxis (Figure 2 and Figure 1– Video 2). Chemotaxis is directed by the external cAMP concentration field, which is determined by the release of internal

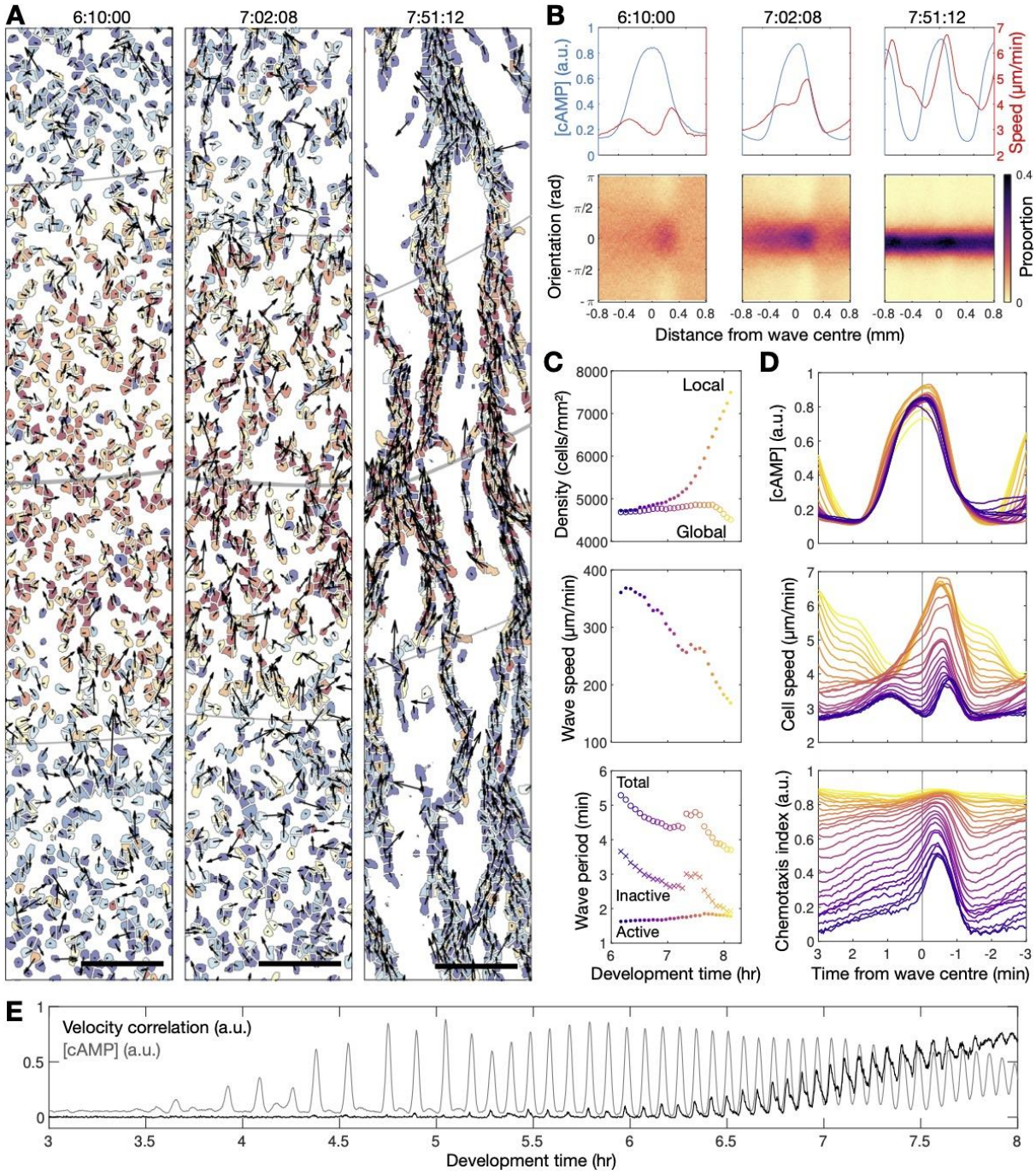

Figure 2: Transition to collective cell motion. A) Snapshots of cell velocities (arrows) and signal states (coloured by [cAMP], as in Fig 1B) surrounding a cAMP wave (travelling from top to bottom) at 3 different time points following spiral wave formation. The inferred wave boundaries and peak are highlighted as grey lines. Scale bar: 100µm. **B)** (top) The mean cell [cAMP] (blue) and speed (red); bottom panels show the orientations of the cells with respect to the direction of wave motion (0 is facing the wave; +/- π facing away from the wave), as a function of distance from the wave centre for the 3 waves shown in A. **C)** The local (mean) and global population density (top), wave speed (middle) and wave period (bottom) for each wave during 6 to 8 hours following starvation. Each data point is coloured by wave number. **D)** The mean cell [cAMP] (top), speed (middle) and chemotaxis index (bottom) across each wave, represented as the time to the wave centre (positive values correspond to behind the wave). Each line is coloured by wave number as in C. **E)** The mean cell [cAMP] (grey) and local velocity correlation (black) between cells within a 400µm² area.

cAMP (reported by Flamindo2) from individual cells. The spatial organisation and motility of cells changed rapidly, occurring around 7 hours following starvation, coincident with the dominance of spiral waves (Figure 2A and Figure 2—Supplementary Figure 1). During this process, cAMP waves

steadily became more frequent, slower and thinner and cells became faster, more directional and persistent in their movement (Figure 2B and 2C). The profile of the mean cAMP pulse in single cells remained constant with each wave. Since the duration of a cAMP pulse (τ) remains constant, and the wave speed (v) decreases, then the wave width ($w = v \times \tau$) also decreases. A thinner wave generates a steeper external cAMP gradient, which may enhance chemotaxis (Song *et al.*, 2006).

To quantify collective cell motion we used the following two measures: (i) the mean chemotaxis index, the proportion of cell movement in the direction of the oncoming wave (Skoge *et al.*, 2014) (Figure 2B,D), and (ii) the local correlation of cell velocity (de Palo, Yi and Endres, 2017) (Figure 2E). Cells consistently moved towards the wave source at wave fronts but remained spatially uniform before 6 hours of starvation, due to random cell motion at the wave rear (Figure 2B -bottom left panel). This is highlighted by a peak in the local correlation of cell motion (Figure 2E) and the mean chemotaxis index (Figure 2D bottom panel) at the wave front, both of which then decay towards zero (indicating random cell motion). For infrequent, fast and wide waves (i.e. circular patterns), the chemotaxis index and local correlation of cell motion reached their baseline values at the following wave front, indicating cells move randomly. This random cell motion disrupts the order in collective cell motion initially induced by the front of the wave. For frequent, slow and thin waves (i.e. rotating spiral waves), the chemotaxis index and velocity correlation significantly change as the cAMP wave frequency increases between 6 and 8 hours following starvation. From 6.5 hours onwards, when the wave period is less than 4.5 minutes, the measures of collective cell motion do not relax back to their previous values by the next wave and hence gradually increase over time to constant, elevated values across the entire wave (Figure 2D and 2E). In parallel, the cell speed at the front of the wave increases incrementally with each wave until it peaks at around 7 µm per minute (Figure 2D 2nd Panel). These data are consistent with models where decreasing the wave period causes cells to gradually become more persistent towards the direction of the wave source and hence gain consistent collective motion (Skoge *et al.*, 2014).

To test the relationship between wave frequency and collective migration in the full population context, we photoactivated bPAC in a small patch of cells at different intervals, and monitored the resultant activation waves (Figure 3 and Figure 3–Video 1). Consistent with our observations shown in Figure 2, cells collectively migrated towards the signalling centre only when the induced wave period was less than 4.5 minutes (Figure 3A). However, photoactivation of cells with a period less than 3.5 minutes did not result in aggregation. We infer that this is because cells cannot relay a steady periodic signal close to their maximum firing rate initially, resulting in a missed wave every second photoactivation event (Figure 3C), leading to the signalling centre becoming “taken over” by another set of period waves. Motivated by the observed change in wave frequency during

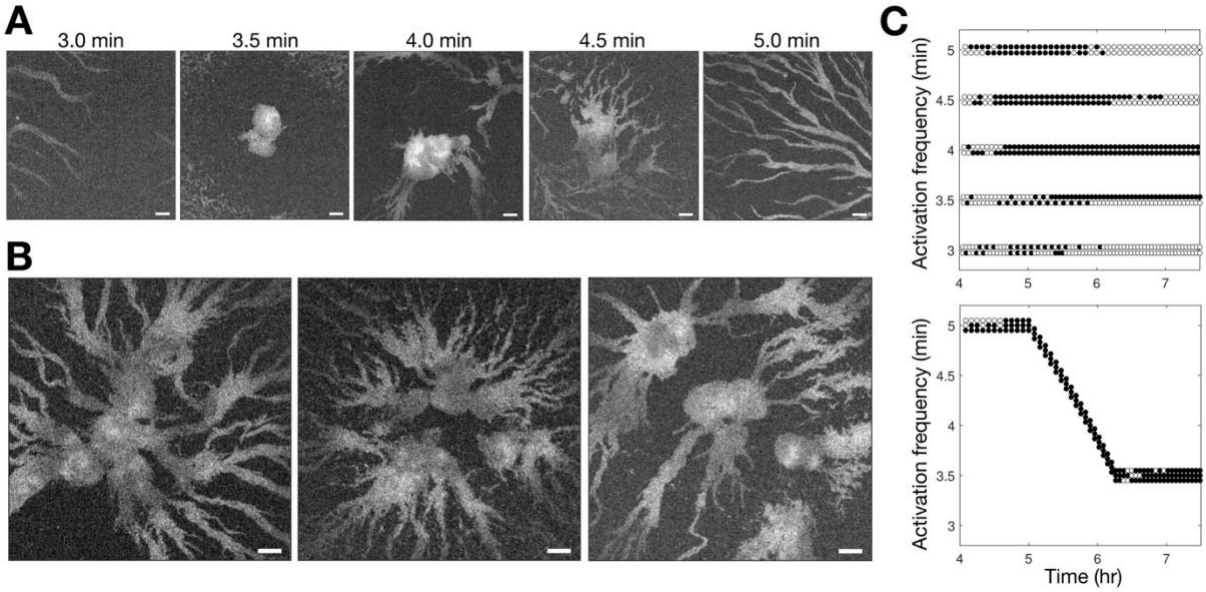

Figure 3: Controlling aggregation by setting the cAMP wave frequency. A) Raw images of a small area of the population subjected to 3 hours of periodic activation of the bPAC optogenetic adenylyl cyclase (with pulses applied at centre of the field of view) at 3, 3.5, 4, 4.5 and 5 minute intervals. Scale bar: 100 µm. **B)** Same as A except that the frequency steadily increased (5 second increments) from 5 minute intervals to 3.5 minutes from 1 hour of periodic photoactivation at 5 minute intervals. Note that the size of the images are larger than those in A. Scale bar: 100 µm. **C)** Time series of the periodic photoactivation protocol for the experiments shown in A (top) and B (bottom). The coordinate of each circle represents the time (x-axis) and frequency (y-axis) of photoactivation, its colour indicates whether it resulted in a relayed circular wave (black) or not (white). Note that the experiments in A are in duplicate, and those in B are in triplicate.

aggregation, we sought to test if it were possible to induce large cell aggregates by photoactivating cells at a faster rate than what we observe experimentally, by reducing the wave period gradually from 5 minutes to 3.5 minutes from 5-6 hours following starvation, rather than 6-8 hours (Figure 3C 2nd panel). This was indeed achievable, resulting in the accumulation of a significantly larger number of cells around the signalling centre and conglomerates of several aggregates (Figure 3B). Our data support the notion that the increase in wave frequency is a crucial determinant of the transition to collective motion. We now turn to the question of how cells generate this increasing wave frequency.

Spiral wave progression

To characterise the regulation of spiral wave dynamics, we imaged and analysed the motion and signalling of individual cells around the spiral core following the onset of spiral formation. The spiral core is the region about which the spiral tip (the end of the activation wave) moves. Based on theory of excitable systems, the spiral tip will sustain itself and the entire spiral wave by virtue of circular motion (Tyson and Keener, 1988; Winfree, 2001). In other words, the circulation of the spiral tip is the organising source of the spiral wave. To better understand the dynamics of spiral tip circulation, and how it relates to the changes in wave dynamics, we tracked the position of the spiral tip and the shape of the spiral wave, from spiral formation to aggregation (Figure 4, Figure 4–Supplementary Figure 1, Figure 4-Video 1 and Supplementary Video 1 and 2). To track tip motion, we mapped the

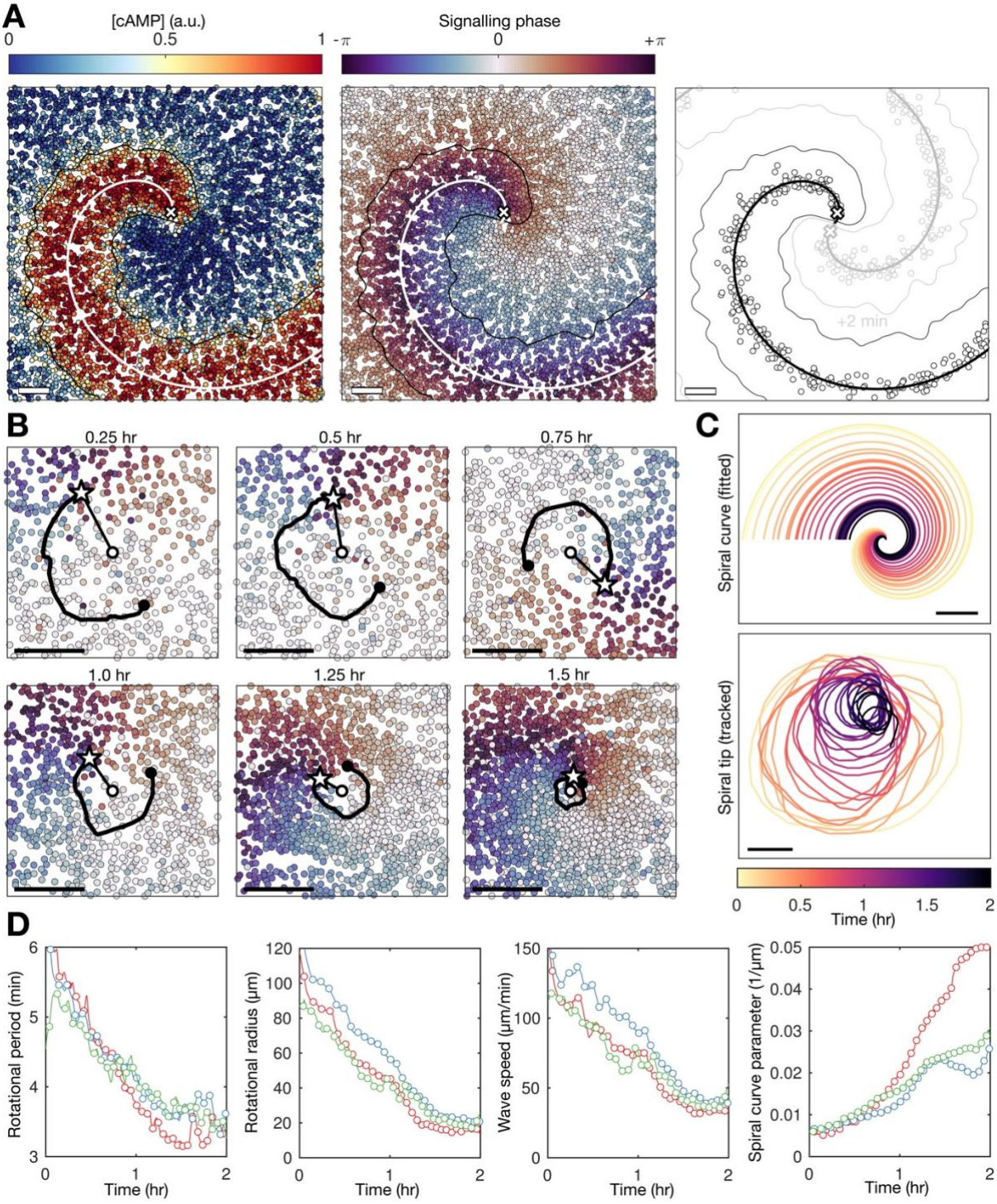

Figure 4 Spiral tip circulation and spiral wave progression. A) The fitted spiral curve (thick line) and predicted wave boundary (thin line) with the spatial distribution of: the internal [cAMP] (1st panel), the signalling phase (2nd panel) and maximally activated cells (phase +/-π) 2 minutes apart (0 min – black, +2min – grey) (3rd panel). Scale bar: 100 µm. **B)** 3 minute tracks (thick black line) of the spiral tip (star) circulating around the pivotal axis/spiral wave singularity (thick white circle) overlayed with cell positions and signalling phase (like 2nd panel of A). Scale bar: 50 µm. **C)** Plots of the fitted spiral curve (mean curve per rotation) (top) and track of the radius of spiral tip circulation (bottom), coloured by time since spiral wave formation. **D)** Time series of the spiral tip circulation rotational period (1st panel), rotational radius (2nd panel), and speed (3rd panel), in addition to the spiral curve parameter (equation (x)) defining the fitted spiral shape in C (4th panel) for each experiment (red, blue and green) since the time of spiral formation. Each circle represents the mean value per rotation.

[cAMP] of individual cells to a phase variable measuring the sequence of changes in the internal

[cAMP] during a cAMP pulse (Figure 4B, Figure 4–Supplementary Figure 1B,C). During a cAMP pulse, this variable increases from 0 (baseline [cAMP]) to +/-π (maximum [cAMP]) and then back to 0. This approach reveals the spiral singularity — or topological defect — which is the point in space around which cells are distributed across the full spectrum of phase states. At each time point, we estimated the spiral tip location as the mean position of maximally activated cells closest to the singularity (Figure 4B). Additionally, we fitted a spiral curve to the spatial distribution of maximally activated cells (Figure 4A and 4C 1st panel).

Spiral waves significantly change in rotation rate and curvature during aggregation, which we refer to as spiral wave progression (Figure 4C and Figure 4-Video 1). These changes in spiral wave structure and dynamics are coupled to changes in spiral tip circulation (Figure 4B-D). The spiral tip rotational period decreased from 5.5 min to 3.5 min. These changes in the rotational period of the spiral tip translate to the changes in the rotation rate of the spiral wave: the decrease in the spiral tip rotation period (Figure 4D 1st panel) is consistent with the decrease in the wave period away from the spiral core that coincides with the onset of collective migration (Figure 2C and 3). The acceleration of spiral tip circulation is associated with spiral core contraction; the radius of circulation steadily reduced from around 100 µm to 20 µm (Figure 4D 2nd panel). Meanwhile, during this contraction, the spiral tip speed decreased from 100-120 to 40-50 µm/min (Figure 4D 3rd panel). Overall, we summarise these changes as the following: the rate at which the activation waves circulate around the signalling centre sets the frequency of global activation waves disseminated from the signalling centre.

How do cells at the signalling centre drive spiral wave progression? To measure the fundamental signalling parameters and how they change over time, we utilised the general theory of excitable media (Tyson and Keener, 1988). *Dictyostelium* cAMP waves can be shown to satisfy this theory (Tyson *et al.*, 1989; Foerster, Muller and Hess, 1990). Our high-resolution datasets now make it possible to apply this theory to understand how spiral waves change during aggregation, independently of the specific equations that model cAMP release, which are still disputed (Sgro *et al.*, 2015; Kamino *et al.*, 2017). According to this theory, the shape of the spiral wave must satisfy a curve that is approximately Archimedean (Methods, equation (2)). The spiral curve depends on a single parameter $k = N_0/\varepsilon D$ (referred to here as the curve parameter) which relates the signalling parameters N_0 (the planar wave speed), D (the signal diffusion constant) and ε (the ratio of the rates of cell inactivation and activation, which we call the cell activation parameter) (Methods, equation (3)). Crucially, the inverse of ε is the measure of cell excitability and specifies the rate at which cells activate. By fitting the spiral curve to the spatial distribution of maximally activated cells at each time point (Figure 4A, 5A, Figure 4–Video 1), throughout spiral wave progression, we obtain a measurement

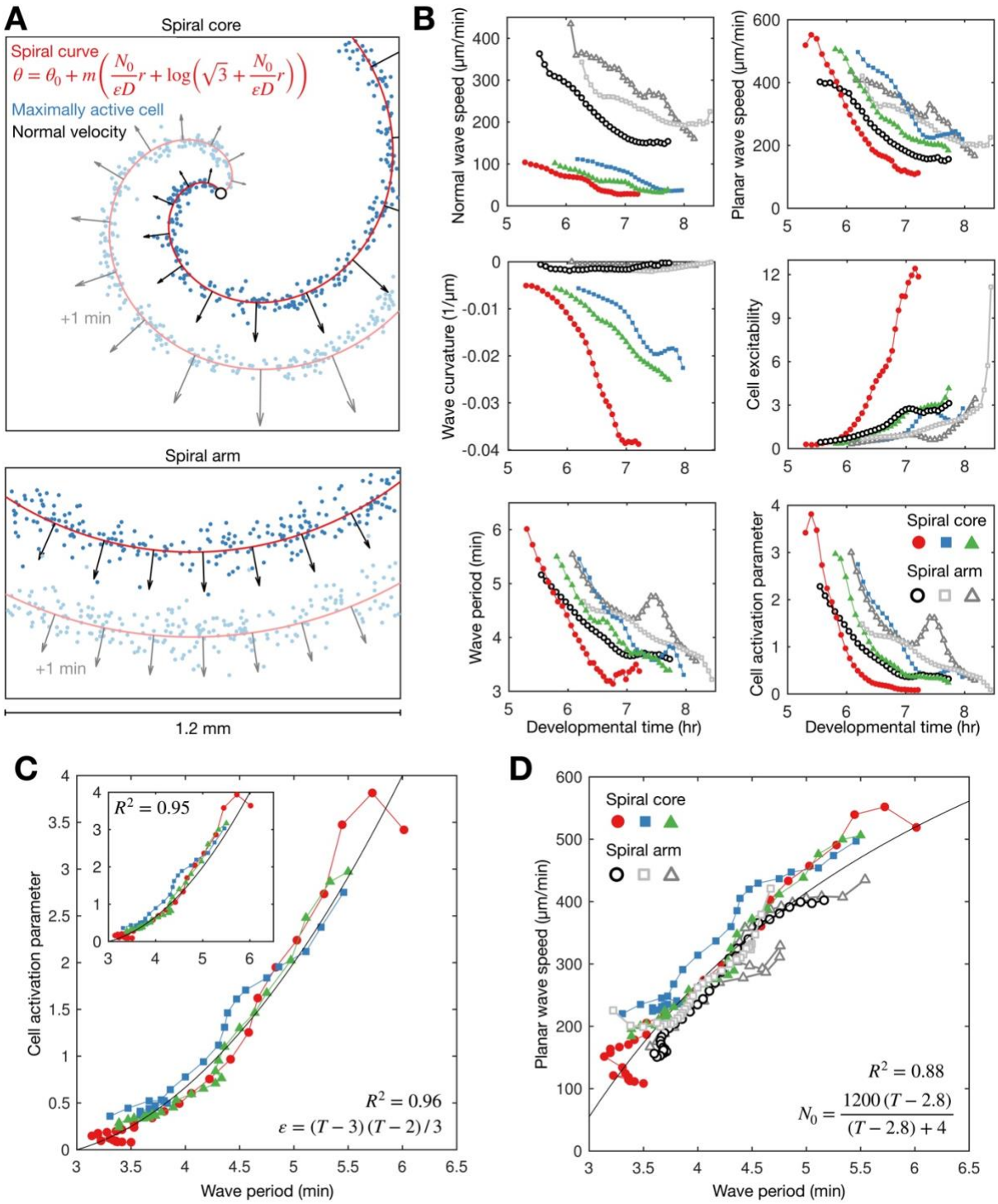

Figure 5: General theory of excitable media – cell excitability is coupled to wave dynamics. A) Representative curve fits (red line) to the distribution of maximally activated cells (blue dots) at (top), and away from (bottom), the spiral core. The normal wave speed is shown as black arrows. **B)** Time series of the measured values of wave characteristics derived from A. For the spiral core, the values were derived from the spiral tip. Coloured lines for wave dynamics at the spiral core. Grayscale lines for waves away from the core. **C)** The cell activation parameter (calculated using the eikonal relation) plotted against the wave period at the spiral core. Inset shows the same plot, but with the activation parameter derived from the curvature relation, together with the fitted quadratic function (black line). **D)** The dispersion relation at (colours), and away from (grey scale) the spiral core, together with the fitted saturating function. The data shown in dark grey are derived from the same experiment shown in Figure 2. Spiral wave data is from the same experiments

of how the cell excitability and planar wave speed changes over time (Figure 5B 2nd column). Specifically, both measures of the cell signalling phenotype can be expressed in terms of spiral wave

properties that we can measure (Methods, equation (4)), such as the normal wave speed and wave curvature (Figure 5B 1st column).

This analysis reveals that the activation parameter and planar wave speed both decrease during spiral wave progression (Figure 5B). Firstly, we find that the planar wave speed halves in value as the wave period decreases towards its minimum (Figure 5D). The theory of excitable media provides the following interpretation: as the wave period decreases, cells have less time to reset between waves, causing slower cell activation and wave speed (the dispersion relation), which gives rise to the deceleration of wave speed during core contraction. This deceleration quantitatively matches the changing wave dynamics away from the spiral core (Figure 2C and 5B), meaning the circulation of the spiral tip determines the wave speed away from the core, in addition to the frequency. Secondly, the theory interprets the increase in spiral wave rotation rate and curvature to be a consequence of cells becoming more excitable over time (Figure 5C). In other words, the spiral waves progress because cells can activate faster. Indeed, although there was temporal variation between experimental replicates, the activation parameter collapses onto a highly consistent curve when plotted against the wave period (Figure 5C), showing how the wave dynamics are strongly coupled to the excitability of the cells. A simple quadratic provides a good fit regardless of derivation used for quantifying the activation parameter (Methods, equations (4) and (5)). In summary, this analysis implies the change in cell excitability is a key element driving spiral wave progression. How does this change in excitability arise?

Hypotheses

Hypothesis 1: density increases excitability. The existing paradigm, based on mathematical modelling, is that spiral wave progression is driven by an increase in cell excitability due to an increased cell density at the spiral core (Hofer, Sherratt and Maini, 1995; van Oss *et al.*, 1996). In this view, the cell excitability increases by virtue of cells accumulating at the spiral core through chemotaxis. Consistent with this paradigm, we measured a substantial decrease in the cell activation parameter (inverse of cell excitability) and increase in cell density during spiral wave progression (Figure 6). The relationship between density and the activation parameter is incredibly sensitive, meaning slight fluctuations in density (such as occurring through random motility) would correspond to dramatic changes in the activation parameter (Figure 6C 1st panel). However, unlike the strong relationship between wave period and cell excitability (Figure 5C and 6C 3rd panel), a causative relationship between density and excitability is not supported by reliable fits (Figure 6C 2nd panel). In addition, our data show that spiral wave progression occurs prior to clear changes in cell density (Figure 6A). Specifically, spiral core contraction and the increase in rotation rate is immediate and steady for around 1.5 hours following spiral wave formation (Figure 6B 2nd panel), while the cell density sharply increases only after around

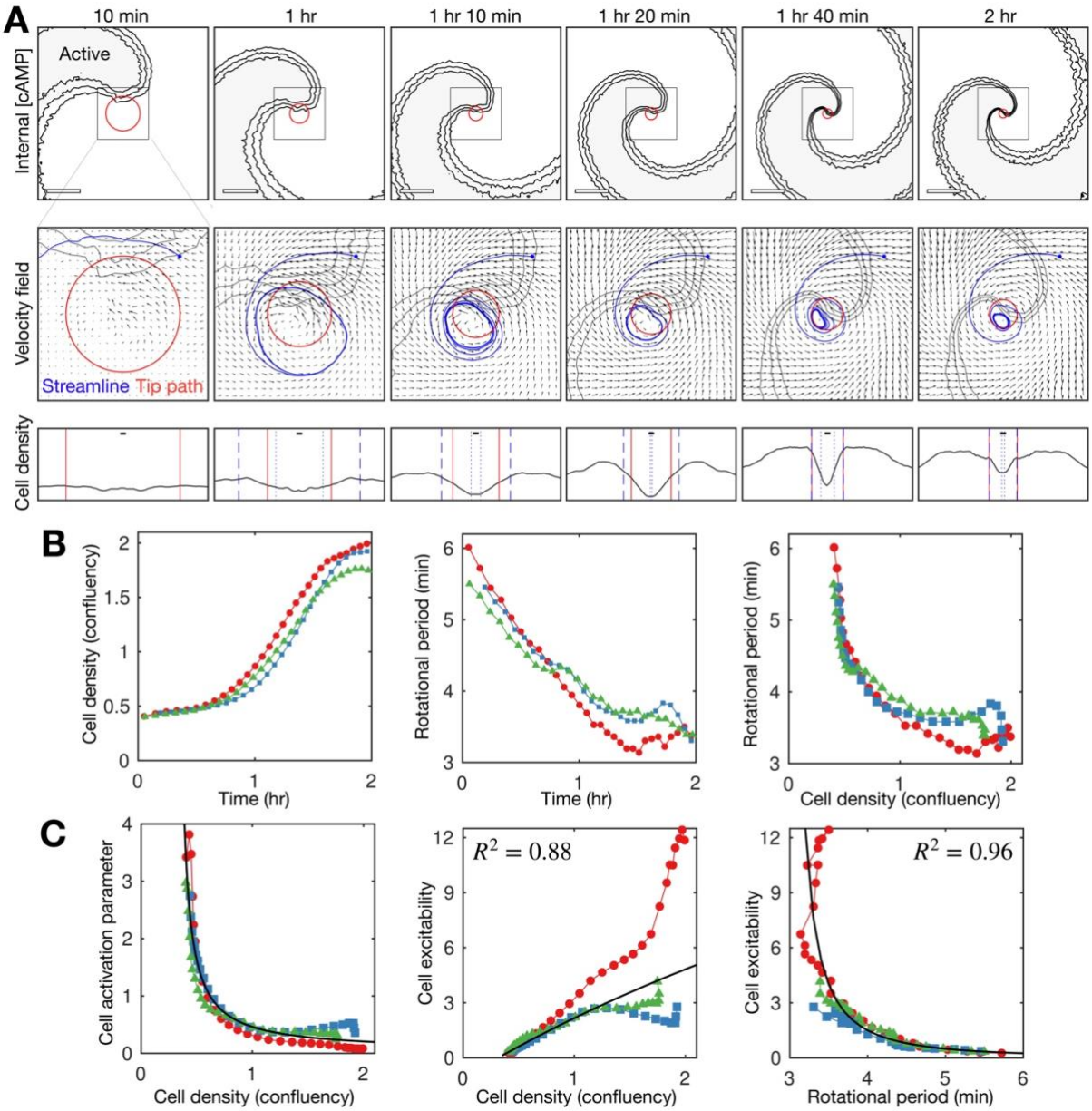

Figure 6: Relationship between cell density and distribution to spiral wave progression. A) Top row: The mean internal [cAMP] around the tip with the mean circulation radius of the spiral tip (red). Scale bar: 200 µm. Middle row: Mean cell velocity field together with a representative streamline, the mean radius of the path of spiral motion (red) and contoured outline of the spiral (grey). Bottom row: cell density together with the mean radius of the spiral tip motion (red) and the minimum (dotted) and maximum (dashed) distance of the representative streamline from the axis of spiral rotation (blue). Scale bar: 10µm (≈ 1 cell diameter). Each plot represents a 5 min average. **B)** Time series of the cell density (fraction cell confluency, estimated with cell area of $\pi\ 5^2$ µm^2) around the spiral core (1st panel) and spiral tip rotational period (2nd panel), together with the relationship between the cell density and rotational period (3rd panel). **C)** Relationship between the cell activation parameter (1st panel) and cell excitability (inverse of the cell activation) (2nd panel) and the cell density. Relationship between cell excitability and wave period (3rd panel). The cell activation parameter (inverse of cell density) structured by cell density and period were fitted with a reciprocal curve ($\varepsilon = 0.04 + \frac{0.28}{n-0.32}$) and quadratic curve (same as in Figure 5), shown as black lines, with their respective R^2 values.

1 hour (Figure 6B 1st panel) once the wave period is below 4.5 mins. Indeed, the rotational period is close to the minimum value before substantial changes in density occur (Figure 6B 3rd panel). Altogether, these observations imply that an increase in cell density is not sufficient to account for spiral wave progression, at least at the onset of collective migration.

Hypothesis 2: cell spatial patterning drives spiral progression. It is conceivable that extending these earlier models (Hofer, Sherratt and Maini, 1995; van Oss *et al.*, 1996) with a more recent model for cAMP release (Sgro *et al.*, 2015) could provide spiral wave progression that is consistent with our data. To test this, we developed a hybrid partial differential equation (PDE) agent-based model (ABM) (see Methods and Supplementary Information) in the same vein as van Oss et al (1996). To explore how cellular reorganisation influences the signalling pattern, we fixed all signalling parameters such that the intrinsic cell excitability does not change. This model reproduced a rotating spiral wave and experimentally observed spatial patterning of cells (Figure 7, Figure 7-Video 1 and 2). In the model, the rotating spiral wave creates a limit cycle in cell motion (see the circular streamline in Figure 6A). Cells collect along the limit cycle via chemotaxis from both inside and outside the path of tip circulation, forming a ring pattern. The emergence of this limit cycle is matched in our data (Figure 6A and 7, Figure 6–Video 1 and 2). In data and model, both the radius of spiral tip circulation and the ring pattern of cells contract over time. In our model, this contraction occurred in the absence of cell-cell physical interactions (i.e. no crowding effects) but not in the absence of cell motion (Figure 7D and 7E 1st panel). These tests indicate that spiral core contraction can be attributed to the spatial reorganisation of cells via chemotaxis towards the circulating wave, but not necessarily due to crowding effects from cells funnelling towards the spiral core. This effect is also observed in data (Figure 6A): the limit cycle is “blunted” at the location of the spiral tip, suggesting that cell chemotaxis is deflected around the external [cAMP] field of the spiral tip, inwards from the edge of the cell ring. Put simply, the tip is deflecting cells inwards.

Since our data point to the contraction of the radius of spiral tip circulation as the driver of spiral wave progression (Figure 4B-4D), our model suggests the following hypothesis for the progression of the spiral wave: as the external [cAMP] field of the spiral tip rotates about the spiral core, it draws cells from the cellular ring inwards, causing a decrease in the circulation radius and an increase in the wave frequency. In this hypothesis, the spiral progression associated with the onset of collective chemotaxis is driven by spiral core contraction.

Our model sufficiently explains spiral core contraction but not spiral wave progression. Specifically, the spiral wave does not increase in rotation rate during spiral core contraction (Figure 7E 2nd and 3rd panel). The speed of spiral tip motion decreases too much to offset the contraction in the radius of circulation (Figure 7E 4th panel). This is a flaw in the model since the increase in wave frequency is the key element of change coinciding with the onset of collective cell migration. By adding an additional component to the model, which allows the excitability of cells to increase over

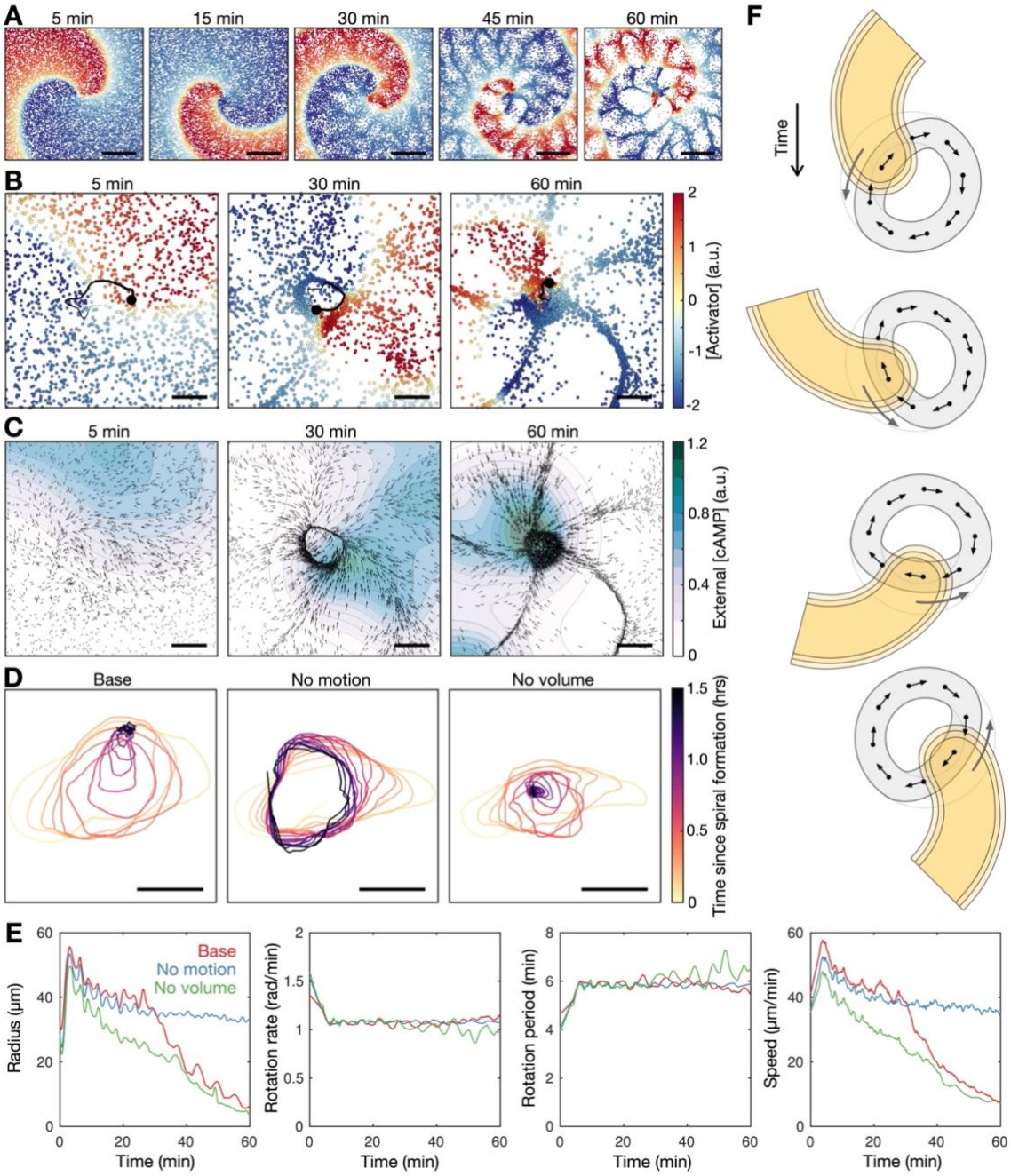

Figure 7: Mathematical model of spiral wave progression. **A)** Simulation of the cell population distribution across space and the concentration of the species governing cAMP release (colour). Scale bar: 500 µm. **B)** Same as A together with the track (black line) of the spiral tip (black circle). Scale bar: 100 µm. **C)** Progression of the external [cAMP] field (colour) with cell velocities (black arrows). Scale bar: 100 µm. **D)** Tracks of the spiral tip (coloured by time) for the original simulation (shown in A-C), a simulation without cell motion (second panel) and without cell volume (third panel). Scale bar: 50 µm. **E)** Time series of the spiral tip circulation radius, rotation rate, rotation period and speed for the simulated tracks presented in D. **F)** Schematic of the mechanism of spiral tip contraction; as the spiral tip travels around the ring pattern of cells (grey), its external [cAMP] field (yellow) directs cell motion (black arrows) inwards from the ring tangent, resulting in the deformation of the cellular ring.

time, this flaw can be bypassed, with the model outputting a strong increase in wave frequency (Figure 7–Supplementary Figure 1 and Figure 7–Video 3).

Hypothesis 3: Wave dynamics drives increased excitability. As the increase in cell density is not sufficient to explain the increase in cell excitability, it is conceivable that the change in excitability is

coupled to the wave dynamics. Based on the relationship in Figure 5C, we propose that cell excitability (i.e. the rate of cell activation) increases as the wave period decreases. This hypothesis states that spiral wave progression is due to positive feedback between cell excitability and the activation wave period: in the context of the spiral wave, which generates periodic waves, the excitability of cells increases the rotation rate of the spiral wave, thereby decreasing the wave period, which raises cell excitability and so forth.

To test this relationship, we first used the quadratic relationship between the cell activation parameter and wave period (Figure 5C) to rederive the relationship between the planar wave speed and wave period (the dispersion relation) in a different context – away from the spiral core. To measure the wave dynamics and structure away from the spiral core (Figure 6B), we exploited that the spiral curve approaches a circle distant from the core (Figure 6A) and fitted an equation for a cone to the time evolution of the spatial distribution of maximally activated cells (Methods). Using this approach, we find a consistent dispersion relation both at and away from the spiral core (Figure 5D).

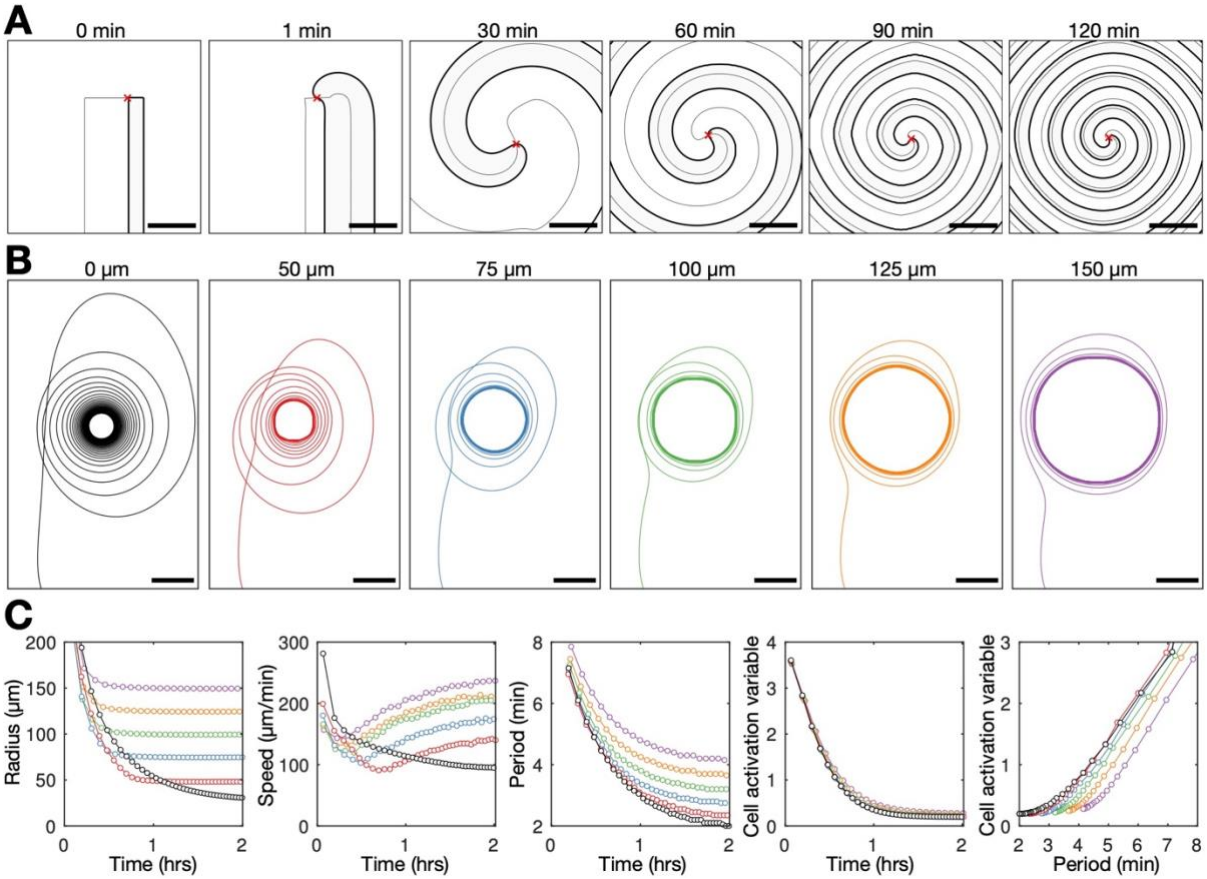

Figure 8: PDE model of spiral progression – coupling cell excitability to wave dynamics. A) Numerical solution depicting the spatial distribution of the external [cAMP] (black contour with shaded interior, $u = 1$) and the inactivator species (grey contour $v = 0.6$). Also shown is the spiral tip location (red cross) estimated by the contour intersections. **B)** Path of spiral tip circulation without (black) and with (colours) a physical block of various sizes (radii shown above). Scale bar: 100µm. **C)** Time series of the spiral tip circulation: radius (1st panel), speed (2nd panel), rotation period (3rd panel) and the cell activation variable (4th panel). Also shown is the relationship between the cell activation variable and wave period (5th panel). The colours represent the measures of circulation for the differently sized physical blocks shown in B.

This relationship was critically dependent on the relationship between cell excitability and wave period.

To test whether the coupling of excitability to the wave dynamics sufficiently describes spiral wave progression, we extended a mathematical model of cAMP spiral waves to simulate the time evolution of the external [cAMP] field over time (Figure 8 and Figure 8–Video 1). We adopted the model by Tyson et al. (Tyson *et al.*, 1989), which is in the general form of continuum excitable media with the dynamics of cAMP release governed by the Martiel-Goldbeter model. Cell excitability is coupled to the cAMP wave dynamics by setting the cell activation variable to be a simple time-dependent function where the variable tends to a baseline value and decreases in response to external [cAMP] (Methods). Figure 8A shows the time evolution of the simulated spiral wave. This solution reproduces features of spiral wave progression such as the rate of spiral core contraction (Figure 8B), increase in spiral wave curvature, increase in the spiral rotation rate and the coupling between the cell activation parameter and the wave period (Figure 8C). The similarity between our experimental data and this model (even with parameter values rounded to the nearest order of magnitude) suggests that the positive feedback between cell excitability and the wave period is a sufficient mechanism driving spiral wave progression (Figure 8–Suplementary Figure 1).

Lastly, the general theory allows us to predict the radius of spiral tip circulation from the measured cell excitability (the curvature relation, Methods equation (5)). Is the change in cell excitability driving the change in circulation radius (Hypothesis 3) or is the radius driving the change in excitability (Hypothesis 2)? If Hypothesis 2 were true, then a change in the measured radius of circulation should precede the change in excitability, and hence the predicted radius. In Hypothesis 3, the circulation radius adapts to changes in cell excitability, in line with previous experiments using caffeine, which inhibits cAMP relay (i.e. reduces excitability), caused a larger radius of circulation (Siegert and Weijer, 1989). Further supporting Hypothesis 3, our data show the change in predicted radius precedes the change in the measured radius, with convergence at the end of spiral wave progression (Figure 5–Supplementary Figure 1). That is, the radius of spiral tip circulation is a consequence, not driver, of spiral wave progression.

Exploring the properties of the radius contraction in the adapted Tyson model shows that the inclusion of a hole in cell density does not hinder spiral wave progression. The spiral wave becomes pinned to the hole, which sets the minimum radius of spiral tip circulation (Figure 8B and Figure 8–Video 2). The wave period reduces (Figure 8C 3rd panel) because the speed of the spiral tip speed remains elevated (Figure 8C 2nd panel) by virtue of an increase in excitability (Figure 8C 4th and 5th panel), compensating for a large radius of circulation (Figure 8C 1st panel). This simulated result

contrasts Hypothesis 2, suggesting that preventing core contraction does not impede spiral wave progression.

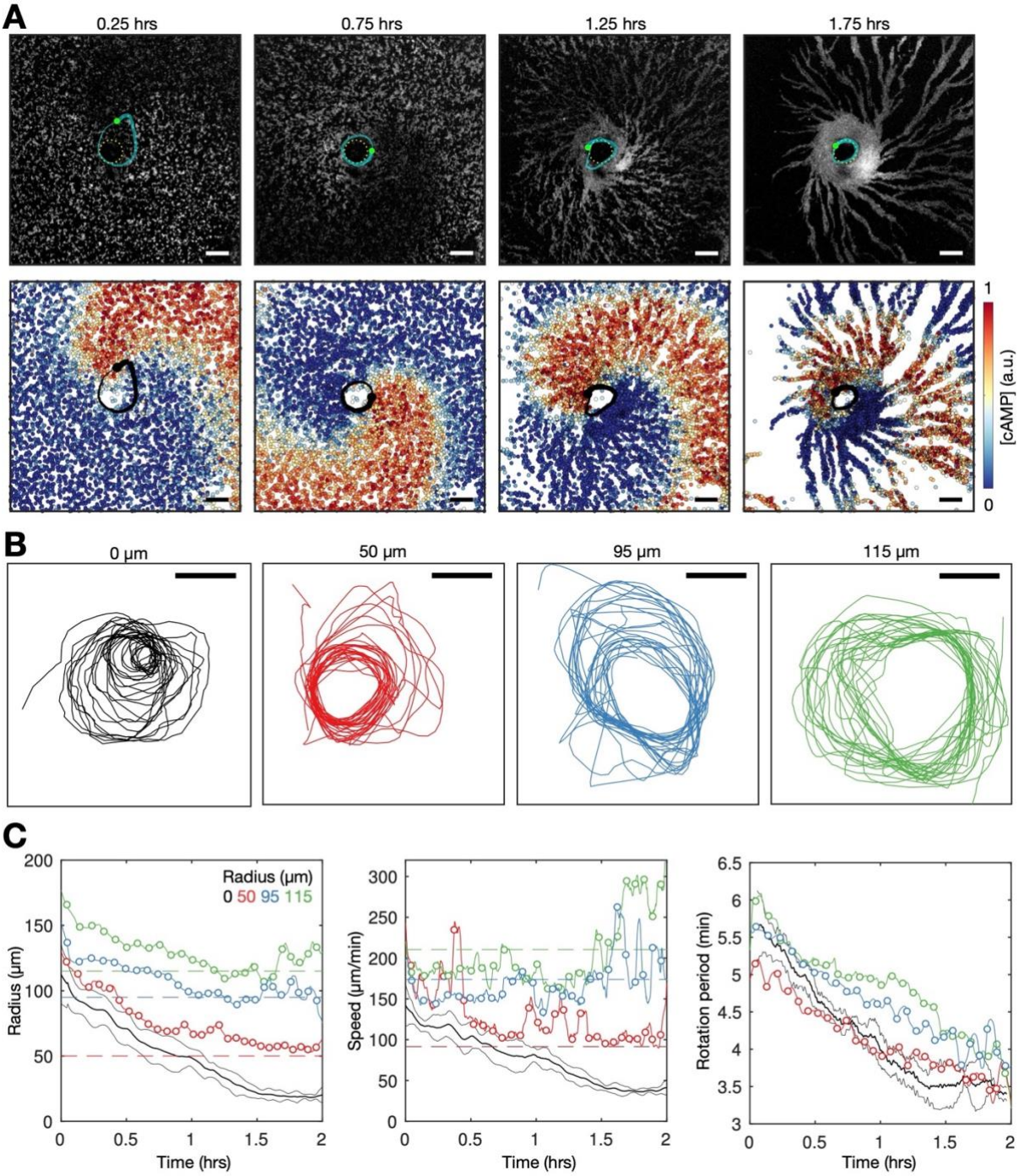

Figure 9: Physical occlusion of spiral core. A) Top: raw images of the population distributed around a physical block (dashed circle) with the spiral tip (green dot) and its track (blue line). Bottom: the spatial distribution of the internal [cAMP] with the spiral tip (black) dot) and its track (black line). Scale bar: 100µm. **B)** Tracks of the spiral tip position for physical blocks of various sizes (radii shown in titles). The control case (no physical block, black) is from a dataset shown in Figures 3-5. **C)** The spiral tip circulation radius (1st panel), speed (2nd panel), rotation rate (3rd panel) and rotation period (4th panel) around physic blocks with different average radii (dashed lines). Also shown is the mean (3 experiment) of the control data without blocks shown in Figures 3-5 (black). Panel 2 also shows the predicted speed (dashed lines) corresponding to the maximum rotation rate 3.5π/6 around the block radius.

Hypothesis testing. We have investigated three hypotheses for spiral wave progression. The prevailing paradigm (Hypothesis 1) is that cell excitability increases due to an increasing cell density, however this model is not supported by our data comparing density with wave period and excitability (Figure 6). The next hypothesis (2) was based on cell rearrangements driving the increase in the spiral wave rotation rate via contraction of spiral tip circulation (Figure 7). The final hypothesis (3) proposes that the wave dynamics change cell excitability (Figure 8). The key difference between these hypotheses is that in Hypothesis 2, the spiral tip contraction is the driver of spiral progression (Figure 7F), whereas in Hypothesis 3, contraction is a consequence (Figure 8–Supplementary Figure 1). Exploring the properties of the models underlying Hypotheses 2 and 3 provides a clear experimental test: to constrain the radius of spiral tip circulation.

To experimentally test the competing hypotheses, we imaged *Dictyostelium* aggregation in the presence of physical blocks (low melt agarose particles with radii ranging between 25 and 150 µm) (Figure 9 and Figure 9–Video 1). Spiral waves can become pinned to the blocks (Figure 9A), with their minimum radius of circulation set by the block radius (Figure 9B). Spiral waves that are pinned to a block cannot fully contract (Figure 9C 1st panel) but nevertheless undergo a steady increase in rotation rate, and hence decrease in wave rotational period (Figure 9C 3rd panel). The circulation rate increases because the spiral tip speed does not decrease to the same extent as the unconstrained spirals (Figure 9C 2nd panel). This observation is in agreement with the model simulations shown in Figure 8, revealing the same effects as in the data – wave speed increased to compensate for larger radius of circulation, generating a reduced rotational period. This observation also reflects our simulations predicting that spiral waves can progress in the presence of physical blocks due to a coupling between the cell excitability and wave dynamics. Together, these observations are consistent with Hypothesis 3, but not Hypothesis 2: the contraction of the spiral tip circulation is a consequence, not a driver, of spiral wave progression.

Overall, our approach provides a clear interpretation of our data, that spiral wave progression results from positive feedback between cell excitability and wave frequency, arising only in the context of the spiral wave pattern (Figure 8–Supplementary Figure 1). That is, from the initial symmetry breaking event (Figure 1–Supplementary Figure 2), the formation of a rotating spiral wave produces stable periodic activation waves, that increase cell excitability, that then increases the spiral rotation rate and hence wave frequency, which then feedbacks onto further increases in cell excitability.

Destabilisation of the spiral wave

To conclude, we now describe the cAMP wave dynamics following aggregation. As development proceeds, more and more cells move into the aggregate. Previous studies show the activation waves are organised as a multi-armed spiral in aggregates (Siegert and Weijer, 1995). How does this

continued cell accumulation affect the cAMP dynamics at the signalling core, and consequently the encoding of information by cAMP waves?

To characterise the single- to multi-armed spiral transition, we monitored the structure and dynamics of the activation waves following ring collapse (Figure 10, Figure 10-Supplementary Figure 1 and Figure 10–Video 1). Single-armed spirals destabilise only once the cellular ring fully contracts. Contraction results in a phase singularity (convergence of all signalling phases) that is fixed at the aggregate centre (Figure 10-Supplementary Figure 1A). The phase singularity and spiral wave are unstable and disintegrate over time. This is likely because the cells are not infinitely small and can only be in one signalling phase at a time. In other words, the cells at the centre cannot activate at a rate necessary to support the full spectrum of signalling phases. The destabilisation process begins by cells signalling out-of-phase with the spiral wave, resulting in the emergence of transient patches of cell activation that gradually increase in number, size and lifetime (Figure 10, around 2 hours following spiral formation). These activation patches rotate about the aggregate while fusing with, and breaking apart from, other activation patches and the original spiral wave, which progressively disintegrates (Figure 10A, 2-3 hours following spiral formation). This process concludes with the appearance of three stable, slow-moving and uncurved activation waves that rotate about the same fixed point at the aggregate centre (Figure 10A, from 3 hours following spiral formation). At this point the signalling regime can be classed as a multi-armed spiral. Although the ring has collapsed, the centre of the aggregate contains relatively few cells (Figure 10-Supplementary Figure 2). At this point there is no phase singularity: the few cells that occupy this central region appear to have signalling phases that are uncorrelated with each other and the surrounding multi-armed spiral wave (Figure 10 Supplementary Figure 1 – last panel). This central region of uncorrelated signalling phases is characteristic of theoretical chimera spiral waves (Totz *et al.*, 2018).

To analyse the transition from the single- to multi-armed spiral, we generated a set of kymographs of cell activation states across the aggregate: one that is cross-sectional, and the others that are circular (Figure 10B). The cross-sectional kymograph shows a disordered signalling regime between 2 and 3 hours following spiral formation, from around 45 minutes after cellular ring closure. In the circular kymographs, both the single-armed and multi-armed spiral waves appear as diagonal lines across space and time (<2 and >3 hours), meaning a constant rotation rate. These data show that the single-armed spiral (<2 hours) has a rotational period of 3.4±0.2 minutes (the minimum cell firing period, see Figures 1, 3 and 4), which is three times faster than the three-armed spiral whose rotational period is 10.1±0.7 minutes and wave period is 3.3±0.5 minutes. This means that the overall frequency with which a cell experiences a wave is the same, because the three-armed spiral provides three waves in its longer rotation period. As such, the frequency of cAMP waves disseminated from

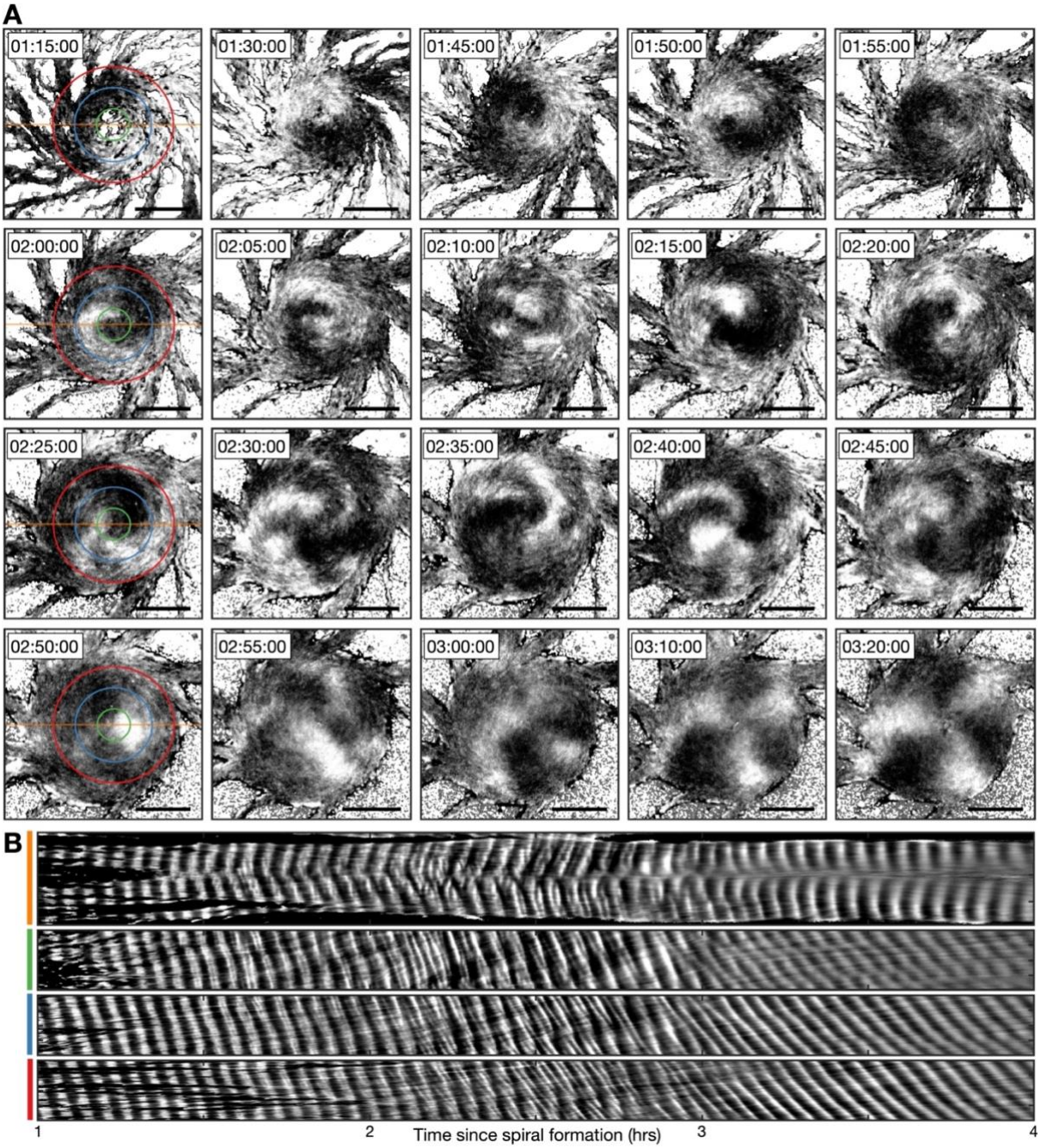

Figure 10: Transition from the single- to multi-armed spiral wave. A) Representative intensity-normalised images of the internal [cAMP] (dark - high, light - low) distributed across cellular aggregates at various time points (labelled) following spiral formation. The images in the left column are annotated with the curves from which the kymographs in B are derived. Scale bar: 100µm. **B)** Kymographs of the data presented in A along a cross-section through the aggregate centre (yellow) and circles with radius 30 µm (green), 70 µm (blue) and 110 µm (red).

the signalling centre, along the streams, remains the same for both signalling patterns. That is, both patterns encode the same temporal information.

Slow- and fast-waves coexist at the outside of the aggregate midway through the transition to the multi-arm spiral. This is visualised as a mixture of lines of two different gradients in the kymograph (Figure 10B, 4th panel, 2-3 hours). This observation suggests that both signalling regimes coexist by the mixing of cells that relay either the single- or multi-armed spiral wave. The multi-armed

spiral wave eventually becomes dominant as the proportion of cells that relay the single-armed spiral wave declines. Altogether, our data suggest that the signalling pattern adapts to the change in aggregate geometry while maintaining an active phase wave that generates waves at the maximum frequency.

Discussion

To determine the properties of signal coding during signal relay, we have carried out a characterisation of collective signalling and cell motion during *Dictyostelium* morphogenesis. Our analysis shows how cell aggregation is coordinated by the dynamics of circulating waves of cell activation at the signalling centre. The circulation rate modulates the speed, frequency and width of long-range periodic activation waves, spatially organised as a spiral. Leading up to aggregation, the circulation rate of the spiral tip gradually increases, resulting in an increase in the global wave frequency and a decrease in wave speed, by virtue of the spiral wave rotating faster and becoming more curved. Using the general theory of excitable media, mathematical modelling and physical perturbations of population structure, our data imply the increase in the circulation rate arises due to positive feedback between the cell signalling pattern and cell signalling state. Specifically, the wave circulation rate is determined by the ability of cells to relay the signal (cell excitability), whilst the ability to relay increases as the circulation rate increases. As such, the information encoding a morphogenetic transition unfolds from positive feedback between the signalling pattern and the cell signalling properties at the signalling centre. Altogether, our results describe how the collective behaviour of 10^5-10^6 cells across several millimetres is organised by the signalling dynamics of a few hundred cells.

This study distinguishes biological activation waves from those produced by idealised mathematical models and chemical reactions (Winfree, 1972). The difference is that biological activation waves can encode information that can be modulated and translated to changes in the spatial organisation and gene expression of individuals beyond the spatial scale of the individual, which can feedback to changes in activation wave dynamics and structure. For *Dictyostelium* aggregation, information is generated locally by the rate of circulation of the spiral tip, and decoded globally by cell chemotaxis. Here, by information we mean the properties of the periodic waves, such as frequency and speed, which are translated by cells into a chemotactic and/or gene regulatory response. Information decoding via cell chemotaxis has been studied at both the single cell and population levels. There are several contrasting views regarding the wave properties which cells interpret for chemotaxis. One view is that the ability for cells to move collectively increases with an increase in wave frequency. Skoge et al (2014) showed, by controlling the frequency of cAMP waves, that the chemotactic index increased as the frequency became maximal (Skoge *et al.*, 2014). This observation is consistent with both our correlative and optogenetic data showing onset of collective migration as the wave frequency approaches the maximum cell activation rate. An alternative view is that cells "count" waves: artificial rotating waves revealed that 4-5 waves at high frequency can induce cell polarity migration (Nakajima *et al.*, 2016). While we cannot rule out a counting mechanism, based on our data here and early data on population measurements of aggregation, in which cells would be

counting upwards of 30 waves before making the decision to collective migrate, any counting mechanism would be context-dependent- for example, using counts above a certain frequency of pulses. An alternative view is based on the wave gradient, where cells move maximally towards steep stationary (Fisher, Merkl and Gerisch, 1989; Song *et al.*, 2006) and/or increasing (Varnum, Edwards and Soll, 1985; Wessels, Murray and Soll, 1992; Nakajima *et al.*, 2014) gradients over time. Again, this view is consistent with our data, where both the wave speed and width decrease as the wave frequency increases, meaning that cells are exposed to a steeper gradient for a longer time. Overall, these different mechanisms are looking at different properties of the wave. What our study shows is that all the wave properties: speed, frequency and width are specified by the circulation of the spiral tip. Specifically, once the frequency is set by the tip, all other features are set by default. Altogether, our study implies that the circulation rate of the signal at the signalling centre is the mechanism of information production, regardless of the specific information-decoding mechanism.

The mechanism by which cell state changes in response to the changing wave dynamics is explained, at least in part, because information contained within periodic waves is also decoded in terms of gene expression. In *Dictyostelium,* and many other systems, gene expression is responsive to the frequency of signalling. Expression of the aggregation genes *pdsA* and *csaA* is sensitive to the changing frequency of cAMP pulses (Masaki *et al.*, 2013; Corrigan and Chubb, 2014). The *csaA* gene is induced during infrequent cAMP signalling, then inactivated as the pulse frequency increases as cells aggregate. The transcription factor GataC displays rapid shuttling between the nucleus and cytoplasm in response to external cAMP oscillations (Cai *et al.*, 2014). This process is low-pass filtered, with nucleocytoplasmic shuttling occurring only when external cAMP oscillations reach a threshold frequency. Here, we describe a mechanism controlling a gradual increase in the global wave frequency. In the light of these findings, it is conceivable that Dictyostelium use high- and/or low-pass filtered transcription factors to exploit the gradual increasing wave frequency to control the timing of gene activation. In this way, the sequential timing of activation of several transcription factors across the cell population can be coordinated by signalling centres that disseminate periodic waves that steadily change frequency over time.

In *Dictyostelium*, the temporal coding of cAMP waves allows cells to sense the extent of cell aggregation through the frequency of activation waves produced by the aggregate, which increases as aggregation progresses. In other words, the temporal code allows for long-range sensing of aggregate progression, which can be interpreted as a non-local quorum sensing mechanism. A potential advantage of this adaptive information coding system is that by moving only towards highly frequent and consistent cAMP waves, effort is then concentrated on migration directed only towards an established signalling centre. If cells were to move maximally towards each initial wave, they would

meander and unnecessarily expend energy while cAMP waves settle to a stable pattern, in addition to missing out on the opportunity to chemotax towards sources of nutrition.

Our data reveals the transition from the single- to multi-armed spiral wave during aggregate progression (Agladze and Krinsky, 1982). In the established aggregate, the single-armed spiral is associated with an unstable signalling phase singularity at the aggregate centre. The multi-armed spiral lacks a clear singularity and instead is associated with relatively small numbers of desynchronised cells at the spiral core. This is the hallmark of the chimera spiral state, a phenomenon yet to be observed in a biological system (Totz *et al.*, 2018). Overall, we view the transition to the multi-armed spiral as an adaption to the change in aggregate geometry to maintain an active phase wave at the signalling centre that generates activation waves at the maximum frequency.

In their physiological context most cell populations, including *Dictyostelium*, are structured in three spatial dimensions. It is not trivial to extrapolate our findings (in the standard 2D plane context) to understand three-dimensional activation waves, owing to the limitless number of self-sustaining wave patterns —the scroll waves—afforded by the extra spatial dimension (Siegert and Weijer, 1992; Winfree, 2001; Durston, 2013). To better understand how biological signals are assembled, sustained and controlled in a more general class of tissues, it would be important to extend the experimental, computational and mathematical approaches outlined in this study to characterise the structure, dynamics and biological effects of cAMP wave patterns that coordinate *Dictyostelium* morphogenesis in 3D.

Supplementary Figures

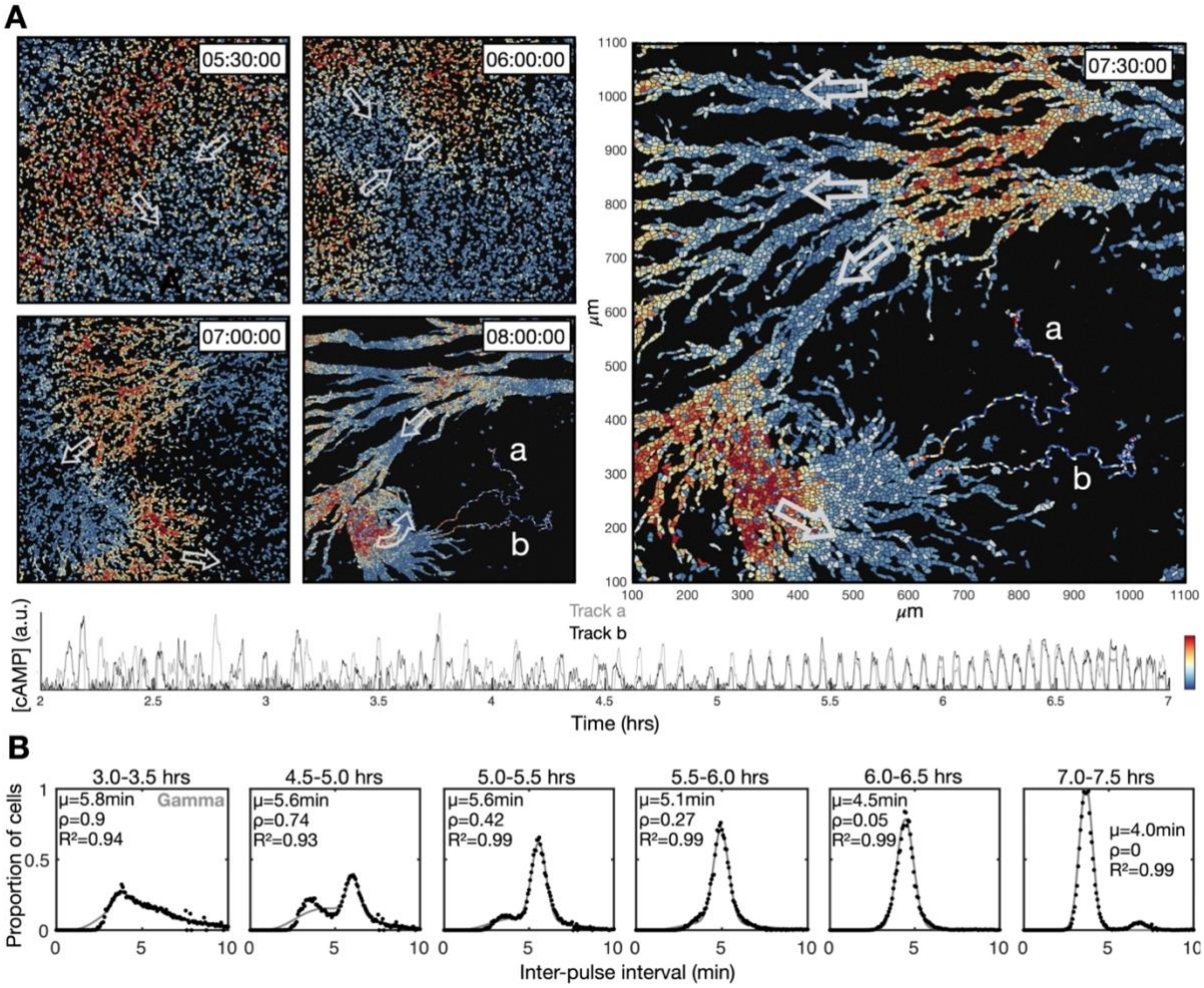

Figure 1 – Supplementary Figure 1: transition to collective cell signalling. These data are derived from a different experiment to that presented in Figure 1. **A)** The distribution of cells and internal [cAMP] (colour) shown at 30 minute intervals following 5.5 hours from starvation, with arrows labelling the direction of wave motion. Also shown at the 7.5 and 8 hour time point are two cell tracks, labelled a and b, whose internal [cAMP] (a.u.) are depicted in the plot below. **B)** Same as 1E, but from a different experiment. The distribution of inter-pulse intervals over different 30 minute time intervals after starvation onset (black) with the mean of each shown by parameter μ, together with a fitted sum of the gamma (weighted by value ρ) and normal (weighted by value 1-ρ) distribution.

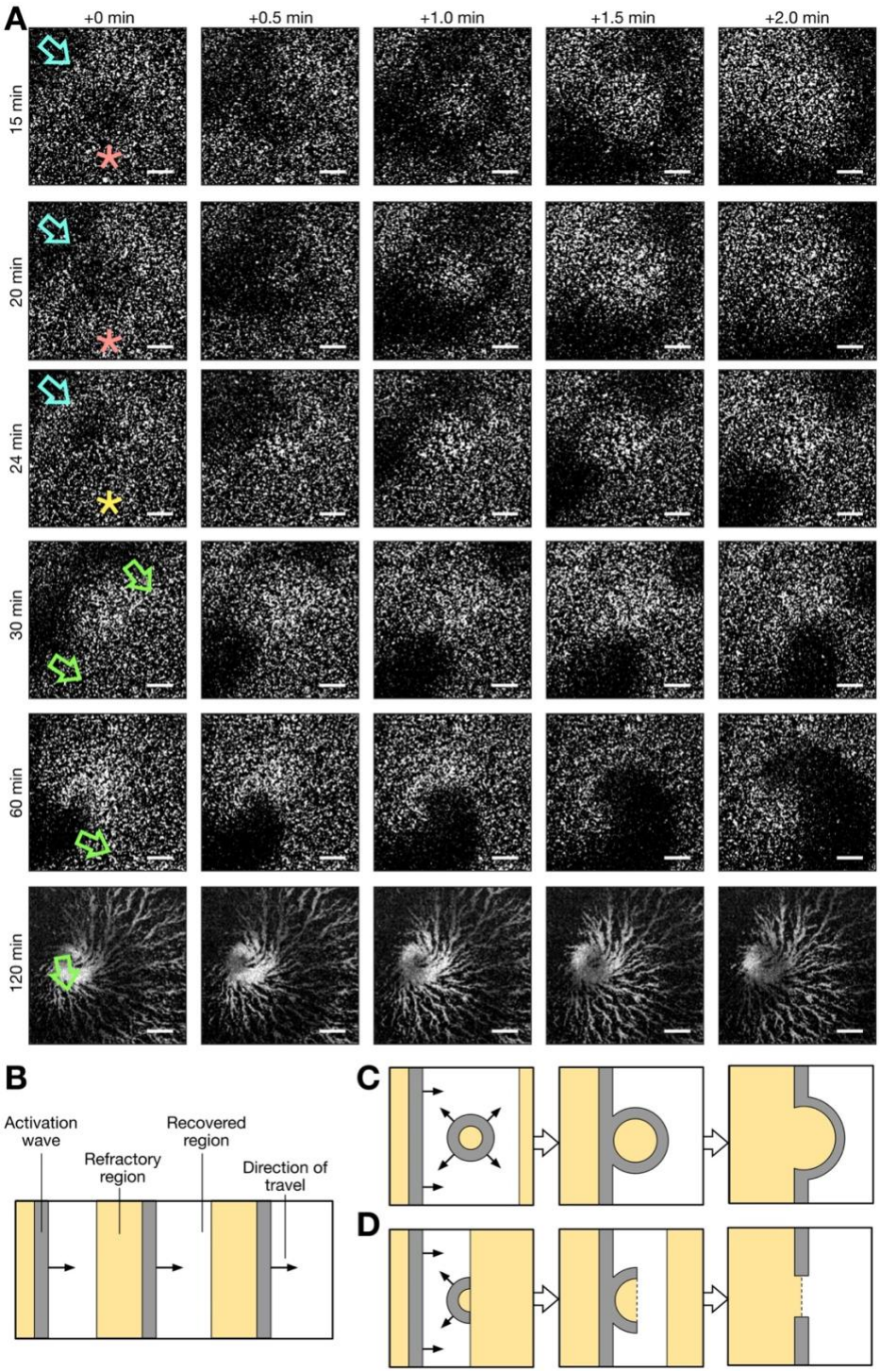

Figure 1 – Supplementary Figure 2: Formation of spiral waves via photoactivation (see Figure 1–Video 3 for the additional clarity). A) A series of raw images (over 2 minute intervals starting from the times labelled at the left of column 1) showing activation waves that: travel from the top right to bottom left corner of the field of view (blue arrow), are circular and result from photoactivation (red stars), are broken/partially circular (yellow star) and rotate. Rows 1 and 2 show a photoactivated circular wave that collides with the oncoming periodic wave. Row 3 shows a photoactivated semi-circular wave (broken) that travels towards, and collides with, the oncoming periodic wave, resulting in a broken wave. Row 4 shows the rotation of both the ends of the broken wave, resulting in two spiral waves. Row 5 shows the dominance of one spiral wave. Row 6 show the aggregate that formed from the dominant spiral wave. Time starts from 5 hours following starvation. Scale bars: 200µm. **B)** Cartoon schematic of the spatial structure of cell activation states for periodic travelling waves. **C)** Same as B, except an activation wave is triggered in the recovered region, resulting in the fusion of the resultant circular wave and periodic travelling wave. This is representative of row 1 and 2 of A. **D)** same as C and B, except that an activation wave is triggered at the border of the recovered and refractory region, resulting in a broken wave shaped as a semi-circle, that collides with the oncoming periodic travelling wave, resulting in a broken wave. This is representative of row 3 of A, which resulted in the formation of a spiral wave (row 4, 5 and 6).

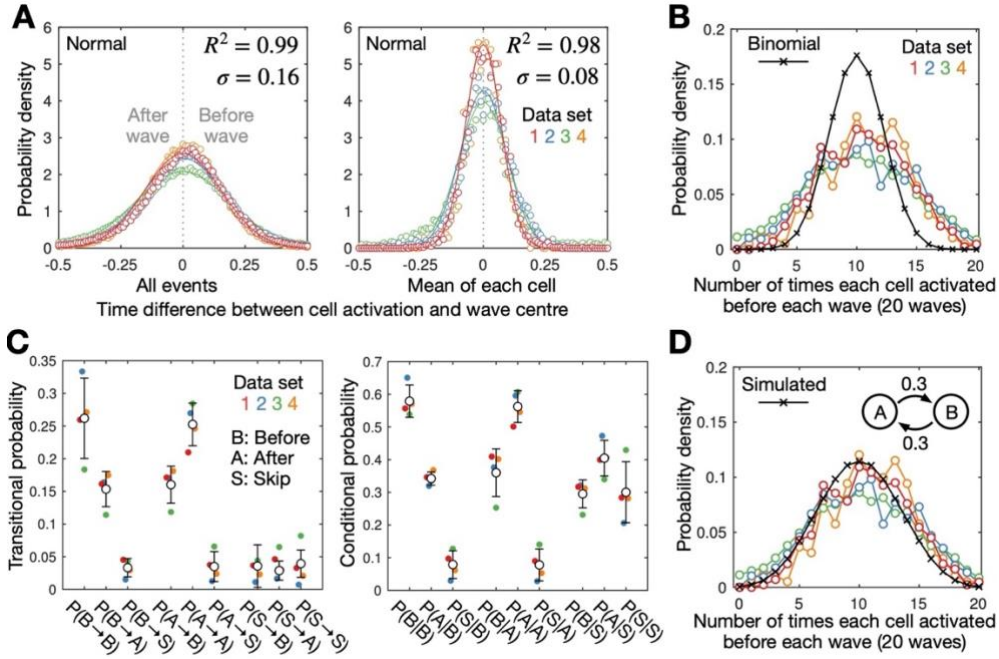

Figure 1 – Supplementary Figure 3: cell-cell variability in activation times. A) Distribution of the time difference between the peak of cell activation and the wave peak for all cell activation events (left) and the mean for each cell (right) (circles) with fitted normal distributions (mean of 0) (line). Also shown is the mean R^2 value and standard deviation of the fitted normal distribution fit for each data set (colours). The mean for each cell provides a normal distribution with a standard deviation that is around half of the distribution for all activation events, suggesting the timing of cell activation is not random. **B)** The distribution of the number of times each cell activated before a set of 20 waves for each data set (colours) compared to the binomial distribution (black crosses). The measured distribution displays a higher spread, indicating cells can be biased to activate before or after waves, suggesting cells are intrinsically heterogeneous or cell activation is history-dependent. **C)** Switching between early and late-firing states. The transitional probability P(X→Y) (left) and the conditional probability P(X|Y) (right) between states X and Y where X,Y=B,A,S; B, A and S represent the states where a cell activates before a wave, after a wave or skips a wave respectively. Shown are the mean (black dots) and standard deviation (error bars) from the same 4 data sets shown in A and B. Cells activate at the same and opposite side of consecutive waves with probability 0.5-0.6 and 0.3-0.4 respectively, with the probability of wave-skipping being 0-0.1. In other words, cells that activate before the wave are slightly more likely to activate again before the next wave, indicating a history dependence, but that this tendency is not fixed. **D)** Modelling bias in firing times: a two-state Markov model with experimentally-derived transitional probability produces a distribution consistent with experimental data. This figure is the same as B except the data is compared to a distribution (black, solid, crosses) simulated from a two state Markov model (inset)–states A (after wave) and B (before wave)–with transitional probability 0.3 for 20 time steps (waves), generated from 10^6 simulations.

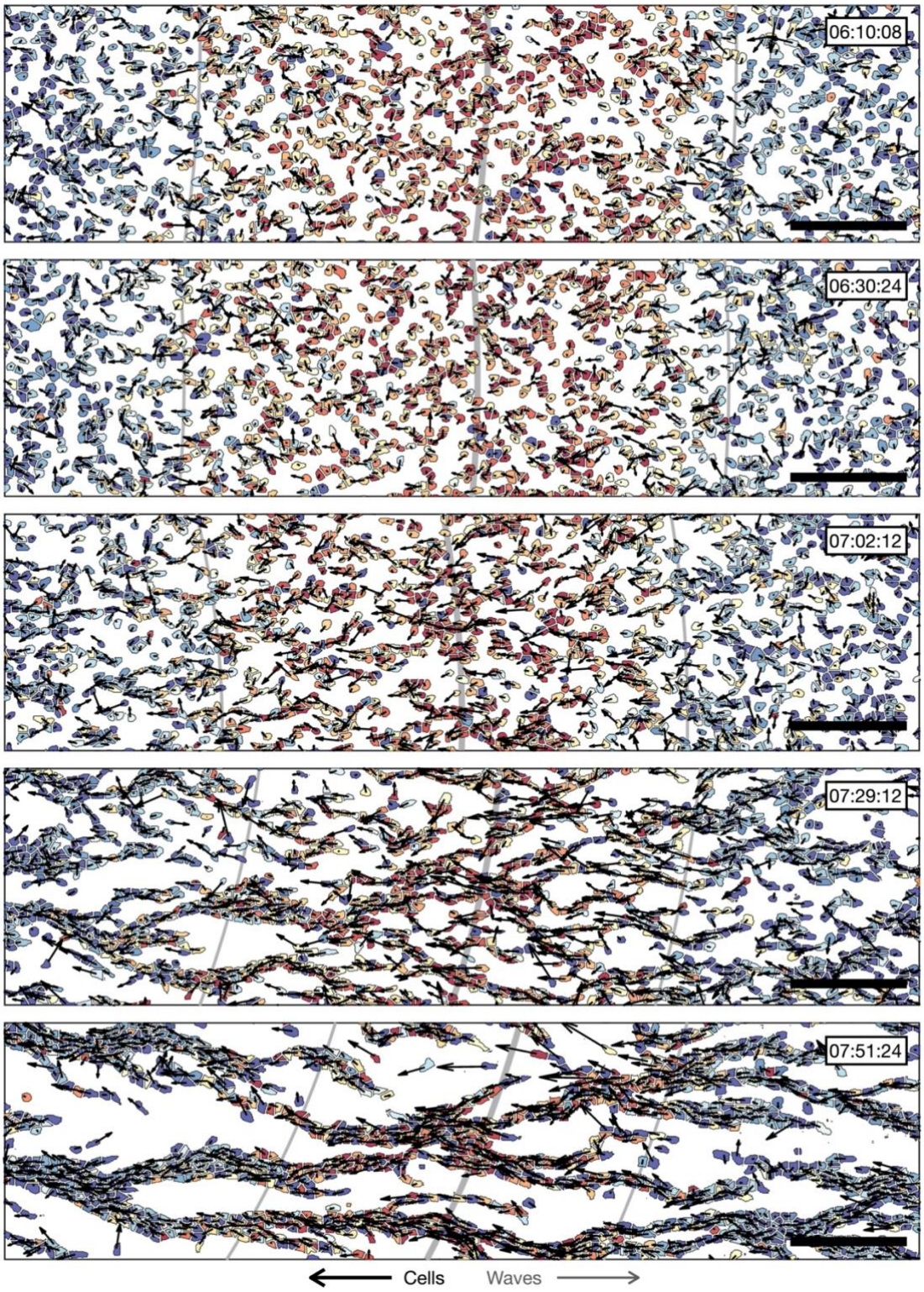

Figure 2 – Supplementary Figure 1: transition to collective cell motion. The distribution of cell velocities and signal states surrounding a cAMP wave (travelling from left to right) at approximately 30 minute intervals different time points following spiral wave formation. The inferred wave boundaries and peak are highlighted as grey lines. Scale bar: 100µm. These data are from the same time series as Figure 2A, showing more timepoints.

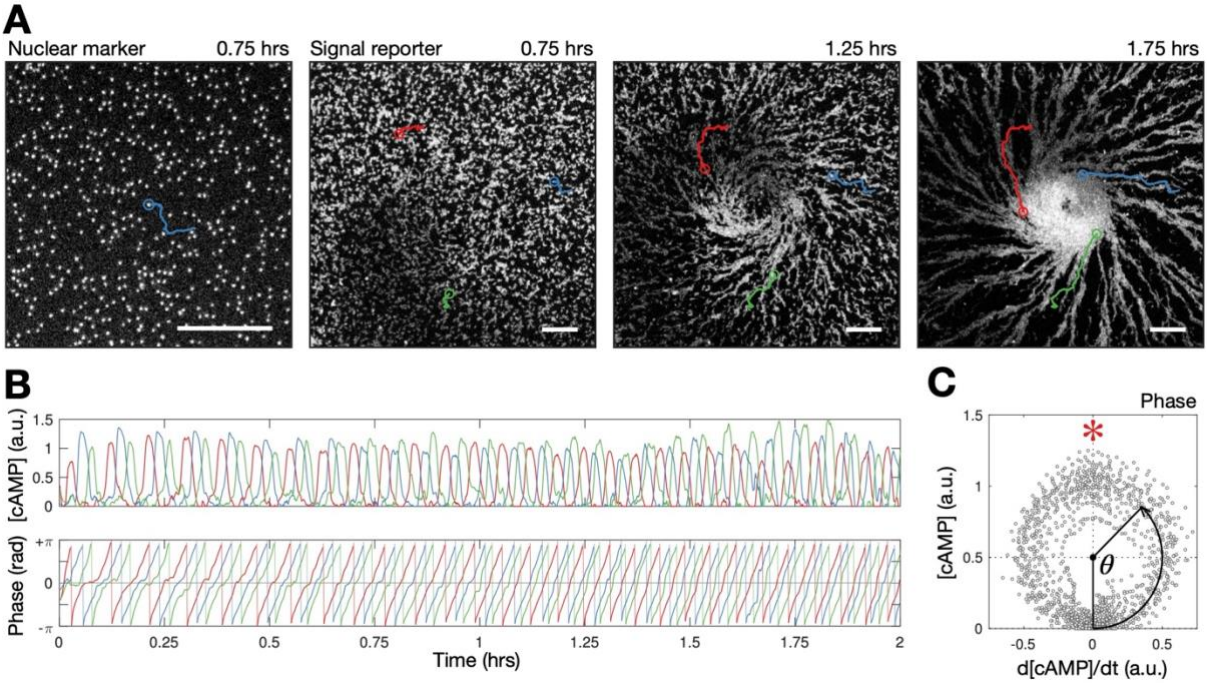

Figure 4 – Supplementary Figure 1 A) Raw images of cell nuclei (left) and cell bodies (right 3 panels) overlayed with cell tracks (red, blue and green). Scale bar: 100µm. **B)** Time series of the internal [cAMP] (a.u.) signalling phase (rad) of the track shown in A. **C)** Phase measurement: the [cAMP] stratified by its change over time.

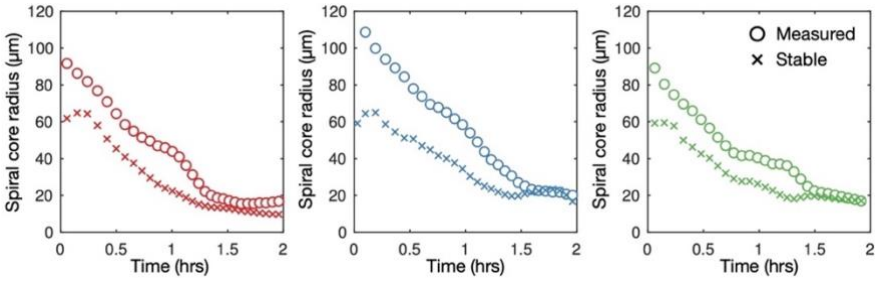

Figure 5 – Supplementary Figure 1: mechanism of spiral core contraction. Time series of the measured radius of spiral tip circulation for the data (3 different experiments) presented in Figure 5 (same colours) (circles) together with the stable radius of circulation predicted using the curvature relation (equation (5)).

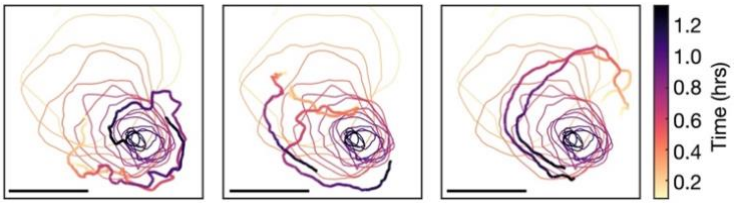

Figure 6 – Supplementary Figure 1: Single cell tracks around the spiral core. The path of spiral tip circulation for one of spirals shown in Figure 4A (Spiral 1) together with single cell tracks of position, coloured by the time since spiral formation. Scale bar: 100µm.

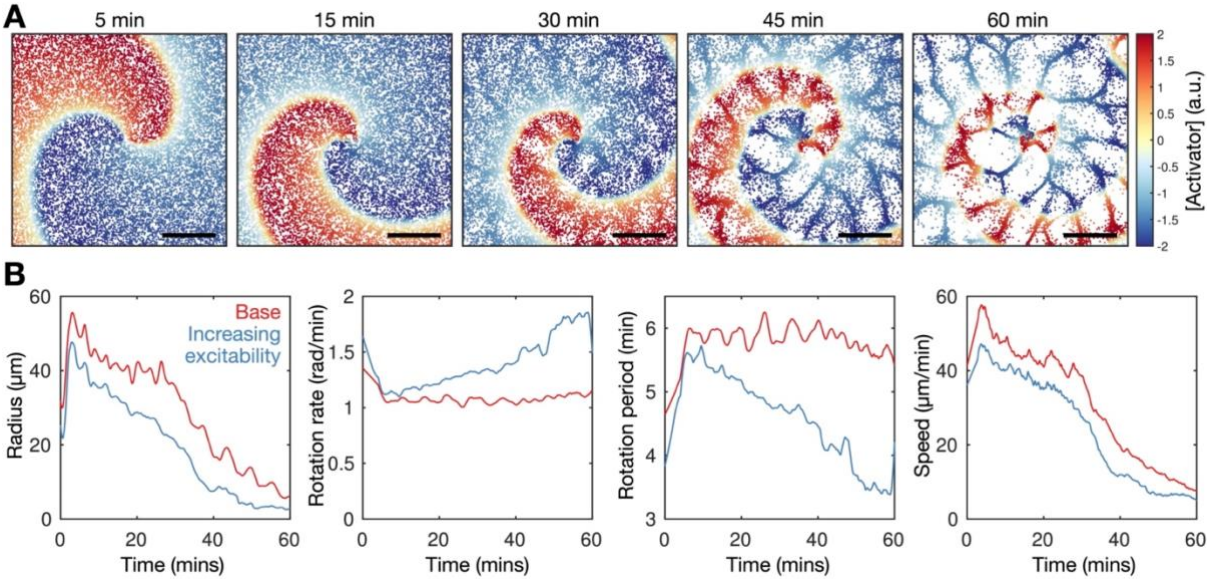

Figure 7–Supplementary Figure 1. Model extension: increasing cell excitability recapitulates spiral wave progression. The rate of cell activation is specified to be a linearly increasing function of time. **A)** Simulation of the cell population distribution across space and the concentration of the species governing cAMP release (colour). Scale bar: 500 µm. **B)** Time series of the spiral tip circulation radius, rotation rate, rotation period and speed for the simulated spiral time for simulation with a constant (red, as in Figure 7) and increasing (blue, as in A) value of cell excitability.

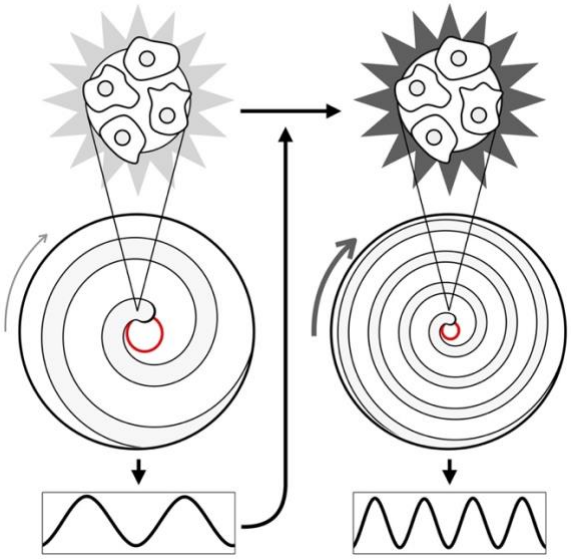

Figure 8 – Supplementary Figure 1: mechanism of spiral wave progression. Schematic showing how the excitability (stars) increases due to an increase in cAMP wave frequency; the cAMP wave frequency increases by virtue of an increase in the spiral wave rotation rate as a consequence of an increase in cell excitability.

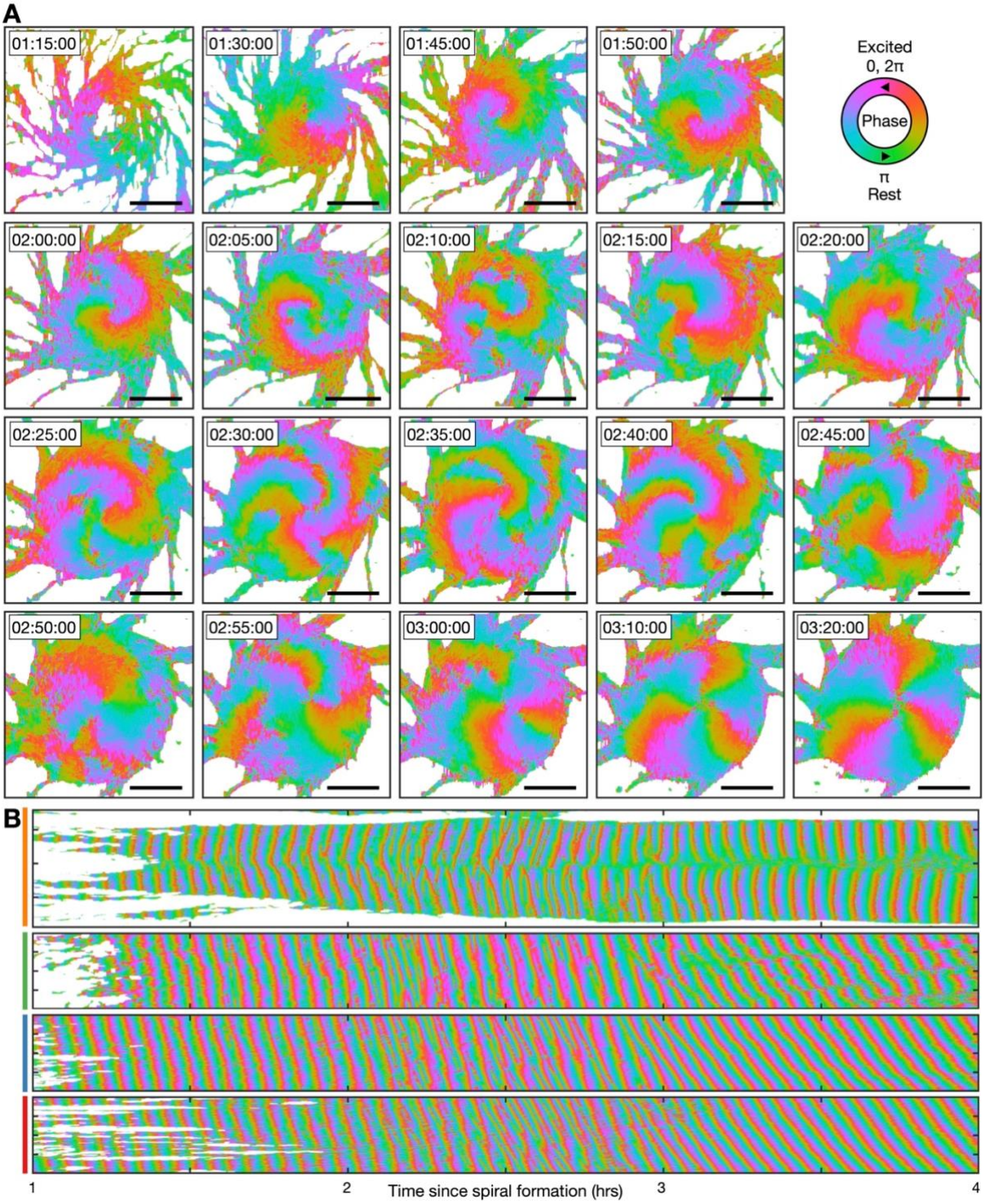

Figure 10 - Supplementary Figure 1: Transition from the single- to multi-armed spiral wave. These data are from the same experiment as Figure 10, except the cell signalling state is represented as the signalling phase (see Figure 3). **A)** Representative images of the signalling phases distributed across the aggregate (red - 0,2π (maximally active) and green - π (rest)). Scale bar: 100µm. **B)** Kymographs of the data presented in A along a cross-section through the aggregate centre (yellow) and circles with radius 30 µm (green), 70 µm (blue) and 110 µm (red), see Figure 10A.

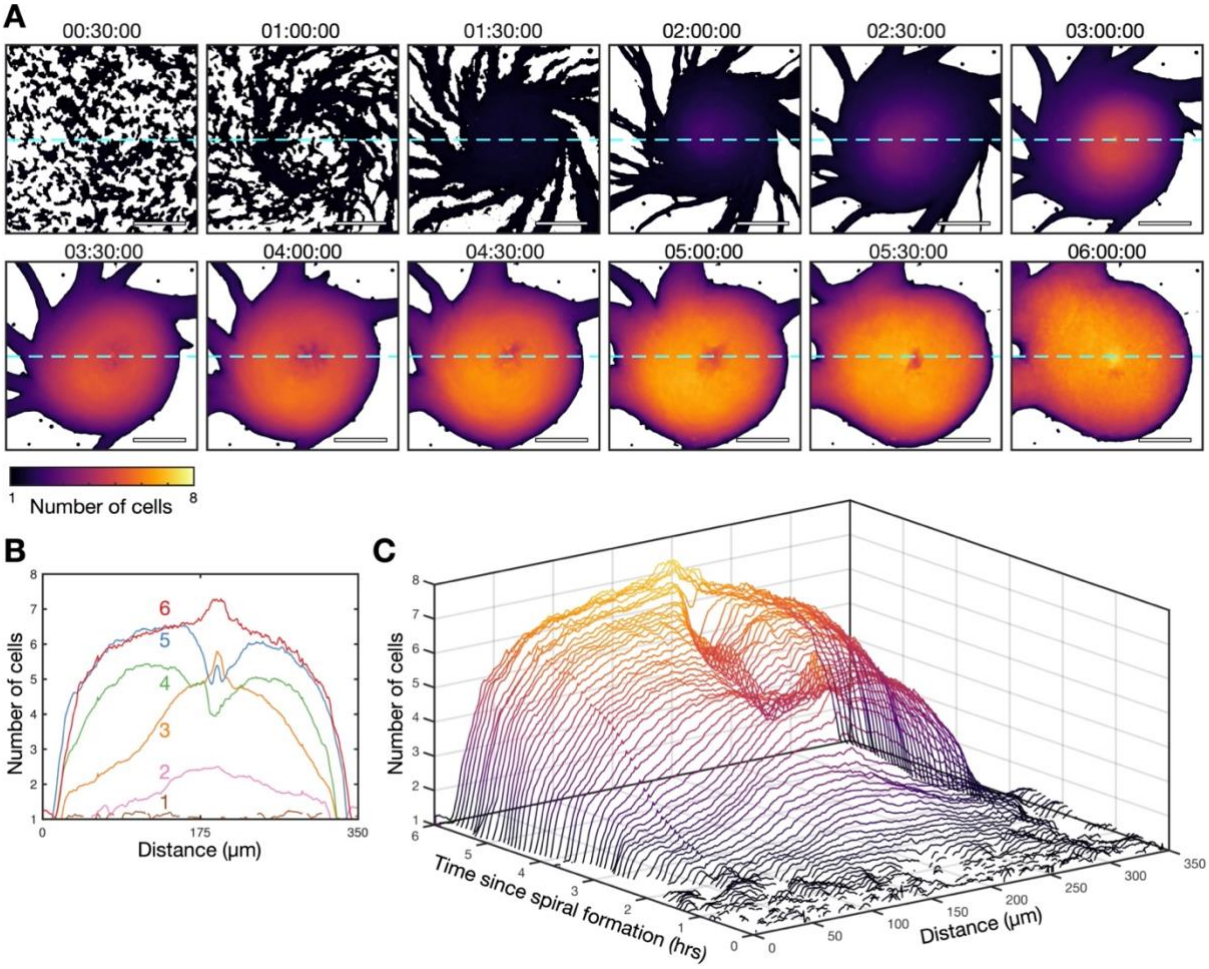

Figure 10 – Supplementary Figure 2: Transition from the single- to multi-armed spiral wave. These data are from the same experiment as Figure 10. **A)** Cell density of the aggregate at 30 minute intervals following the onset of spiral formation coloured by the mean intensity of an individual cells. Scale bar: 100µm. **B)** The cell density of the aggregate along a cross-section through the aggregate centre (dashed light blue line in A) at 1 hour intervals (labelled and in different colours) following the onset of spiral formation. **C)** Waterfall plot of the intensity of the aggregate along a cross-section through the aggregate centre (dashed light green line in A) at 10 minute intervals following the onset of spiral formation, coloured by the aggregate intensity (same as A).

Materials and Methods

Generation of cell lines

Dictyostelium AX3 cells were engineered to express Flamindo2 and H2B-mCherry from safe-haven genomic locations for stable and uniform expression. Flamindo2 is a cAMP biosensor (Odaka *et al.*, 2014; Hashimura *et al.*, 2019) with a fluorescence intensity that is inversely proportional to internal cAMP levels. A codon-optimised sequence encoding the Flamindo2 reporter was knocked-in to the a*ct5* locus for stable and uniform expression (Paschke *et al.*, 2018; Tunnacliffe, Corrigan and Chubb, 2018). H2B-mCherry, knocked into the *rps30* locus, labels the nucleus for cell tracking at high cell densities (Corrigan and Chubb, 2014). For light activation of cAMP signalling, we used the light-activatable adenylyl cyclase, bPAC (Stierl *et al.*, 2011). A codon-optimised bPAC cDNA was cloned into the extrachromosomal expression vector, pDM1203, then transfected into the *act5*-Flamindo2 cells.

Cell handling

Cells were grown at 22ºC in 12 ml of Formedium HL5 medium supplemented with penicillin and streptomycin in 10 cm tissue culture dishes. Cultures were diluted to 25% of their density each day to stop cell entry into stationary phase. Cells were not used beyond 9 days of culture. For development, log-phase cells at 80% confluency were washed and resuspended in KK2 (20 mM KPO_4 pH 6.0), and then plated on 1.5% agar at between $4x10^3$ and $5x10^3$ cells per mm^2. After 1 hour in a humidified chamber, a 1.2cm x 1.2cm slab of agar was cut and gently placed cell-face-down onto a glass imaging dish (Bioptechs deltaT), and then immediately submerged in silicon oil to prevent desiccation. To incorporate physical blocks into the cell aggregation field, we sprinkled low-melting point agarose powder onto the agar bed before it had set, prior to the addition of cells.

Cell imaging

Cells were imaged at 22ºC on a custom-built inverted wide field microscope (Cairn Research) with 470 nm and 572 nm LED light sources (Miermont *et al.*, 2019). This was equipped with a Prime 95B CMOS camera (Photometrics) and 10x UplanFL N objective (Olympus). A 1.2mm x 1.2mm area was imaged at resolution $1\mu m^2$ per pixel every 4 seconds for 8 hours from 2 hours after starvation. To image cell motion and signalling about the spiral core, including the experiments with the physical block, we imaged a 1.2mm x 1.2mmm area for 2 hours following from 5 to 6 hours after starvation. This process required monitoring cAMP wave patterns in real time, and identifying waves that start to rotate about an axis.

Photoactivation

For light activation of cAMP signalling, we used bPAC-expressing *act5*-Flamindo2 cells and a 3i spinning-disk confocal microscope with a 10x objective and Prime 95B CMOS camera (Photometrics). To initiate periodic cAMP waves, cells contained within a circular area with a ≈100 µm diameter were pulsed with 488nm light for 1 second, at intervals to mimic physiological cAMP pulsing. Flamindo2 images (excitation 515nm) were collected throughout the pulse sequence, every 5 seconds. To initiate a rotating spiral wave, we repeated the photoactivation protocol above, except that cells were photoactivated at an operator-controlled location and time points. At a wave period of around 5 minuets, circular wave patterns were induced at around 3 minutes after the previous waves, whereas the asymmetric wave patterns (resulting in the broken and hence spiral wave) were induced around 2 minutes after the previous wave.

Cell tracking and measuring cell signalling states

The following image analysis pipeline was implemented in Matlab 2020b. To track the position of individual cells from image sequences, the IDL particle tracking algorithm (Crocker and Grier, 1996) was applied to the cell nuclei channel (H2B-mCherry) of the image stack. The velocity of each cell at each time point was estimated by the first derivative, second order, central finite difference of cell position. To measure the mean fluorescence intensity of each tracked cell, watershed segmentation (the Fernand Meyer algorithm) seeded from the tracked cell positions, was applied to the cell body channel (Flamindo2). To infer internal cAMP levels (non-dimensional), the tracked mean fluorescent intensity of each cell was normalized and smoothed using Matlab's Savitzky-Golay finite impulse response smoothing filter. Two measures were used to identify cAMP pulses: (i) the similarity between the normalized intensity and a square pulse of length 2 minutes and (ii) the signalling phase φ. Variable φ was estimated by stratifying the time series of the internal cAMP level c by its time derivate $\dot{c}$ (estimated by the first derivative, second order, central finite difference). The value of φ is set as the angle around the point $c = c^*$ and $\dot{c} = 0$:

$$\varphi = 2\ \tan^{-1}\frac{c-c^*}{c+\sqrt{(c-c^*)^2+c^2}}\ .$$

In addition to the time series of the inferred cAMP levels, we recorded the time points of the maximal cAMP level during each pulse, and the time points of cell activation ($\dot{c} > 0$) and deactivation ($\dot{c} < 0$), measured by the time point where the cAMP levels are half-maximal.

To quantify the internal [cAMP] signalling and phase field following aggregation, we tracked the fluorescence intensity of each individual pixel as a function of time, over the entire 2D image sequence. The fluorescence intensity time series was oscillatory and typically increased over time. We used Matlab's Savitzky-Golay finite impulse response smoothing filter to separate the oscillatory and

background component of the signal. The background component was used to estimate the cell density of the aggregate. The oscillatory component was used to estimate the spatial distribution of signalling states and phases across the aggregate, using the same technique described above.

Activation wave curve fitting

To quantify the evolving dynamics of the spiral wave, we first estimated the location of the spiral phase singularity at each time point as the central point of a circular region of radius 100µm with the largest variance in internal [cAMP] across each cell. The location of the spiral tip was estimated by the mean position of 5 maximally activated cells closest to the location of the phase singularity. We estimate the axis of rotation at each time point by fitting a circle to the track of the spiral tip, half a revolution backwards and forwards in time. Using the Matlab function fit, we fit the spiral curve given by equation (2) to the spatial distribution of maximally activated cells, starting from the axis of spiral tip circulation (Tyson and Keener, 1988). To achieve this, we determined the magnitude (r in equation (2)) and orientation (θ in equation (2)) of the vector extending from the axis of spiral rotation to the location of each maximally active cell. This fit provides the spiral orientation (θ_0 in equation (2)) and curve parameter (k in equation (2)).

Away from the spiral core, the time and place of activation for each cell was clustered in three dimensions (two spatial, one temporal) using the DBSCAN (density-based clustering of applications with noise) algorithm as a means to identify cells with correlated signalling states (e.g. during the propagation of cAMP waves) and also, by exclusion, the cells that activate independently. This approach reveals the clusters of cell activation associated with each cAMP wave. For each wave, we estimated the dynamic curve of the wave by fitting an equation for a cone ($t - t_0 = N\,r\,, r = \sqrt{(x - x_0)^2 + (y - y_0)^2}$, where t_0 and (x_0, y_0) is spatiotemporal origin of the wave) to the time evolution of the spatial distribution of maximally activated cells . The slope of each of the cone fitted to the signal peaks was used to deduce the speed of each wave.

Quantifying cell motion

To estimate the mean cell velocity field and density around the spiral wave, we measured the mean velocity and total number of cells at regular lattice areas (step size 10µm) in the reference frame that rotates with the fitted spiral parameter θ_0 (Figure 6–Video 2). The streamlines across this field were analysed using the Matlab function streamlines.

To analyse the behaviour of single cells during stable periodic waves, the fitted cone equations were used to estimate the mean internal [cAMP] and velocity of each cell as a function of distance

from the wave centre. This allows an estimation of measures such as the angle difference between the direction of wave travel and cell motion, for each cell:

$$\cos^{-1}(\widehat{\boldsymbol{v}}_i \cdot \widehat{\boldsymbol{w}}\,(\boldsymbol{X}_i))$$

where $\widehat{\boldsymbol{v}}_i$ is the normal velocity of cell $i = 1, \ldots, N$ and $\widehat{\boldsymbol{w}}(\boldsymbol{X}_i)$ is the normal velocity of the cAMP wave at the location of cell i, $\boldsymbol{X}_i$. The following two formulae were used to measure collective cell motion: (i) the mean chemotaxis index (the proportion of cell movement in the direction of the oncoming wave) as a function of distance from the wave:

$$\frac{1}{N_{\Omega_j}} \sum_{i \in \Omega_j} \widehat{\boldsymbol{v}}_i \cdot \widehat{\boldsymbol{w}}\,(\boldsymbol{X}_i)$$

where Ω_j represents the subset of cells (subset size N_{Ω_j}) located at a distance $j \times 10$ µm ($j = \cdots -1,0,1, \ldots$) from the wave centre, and (ii) the local correlation of cell velocity:

$$\frac{1}{N} \sum_i \frac{1}{N_{\Phi_i}} \sum_{j \in \Phi_i} \widehat{\boldsymbol{v}}_i \cdot \widehat{\boldsymbol{v}}_j$$

where Φ_i denotes the subset cells (subset size N_{Φ_i}) within a 50 µm radius of cell i (de Palo, Yi and Endres, 2017). Local cell density was measured by the mean density of cells within a 60 µm radius of each cell.

General theory of excitable media

This section outlines the elements of the theory we have used, and we used these to interpret spiral wave progression.

The eikonal relation dictates how the normal speed along the wave front N changes due to wave curvature K:

$$N = N_0 + \varepsilon\, D\, K\,, \quad (1)$$

where N_0 is the planar (no curvature) wave speed, D is the signal diffusion coefficient (which we assume remains constant) and ε is the ratio of the rates of cell inactivation and activation (which we call the cell activation parameter). For a wave extending to the pivotal axis, the solution to equation (1) is accurately approximated by the following curve (in polar coordinates, $x = r\ \cos\theta(r,t)$, $y = r\ \sin\theta(r,t)$):

$$\theta \approx \theta_0(t) + m\big(k(t)r + \log\big(\sqrt{3} + k(t)\,r\big)\big)\,, \quad (2)$$

where m is a constant. Parameter k (the curve parameter) defines the curvature of the wave and θ_0 is the spiral angle of rotation, with rotation rate, $\omega = \dot{\theta}_0$. We fit equation (2) to the spatial distribution of maximally activated cells at each time point, throughout the entire progression of the spiral wave. The fit is accurate for all time points, which validates the use of the theory of excitable media even though cells are discretely distributed across space. This fit provides a measurement of the time

evolution of the curve parameter k, rotation rate ω and hence the wave period $T = 2\,\pi/\omega$ (Figure 4D). The value of k relates the planar wave speed to the cell excitability:

$$k = \frac{N_0}{\varepsilon\, D} \quad , \qquad (3)$$

Substituting equation (3) into equation (1) for N_0 allows the cell activation parameter ε and planar wave speed N_0 to be expressed in terms of variables that can be directly measured from data:

$$\varepsilon = \frac{1}{D}\frac{N}{k+K}\,, \qquad N_0 = \frac{N\,k}{k+K}\,. \quad (4)$$

Consistent with the traditional paradigm of spiral wave progression (Hofer, Sherratt and Maini, 1995; van Oss *et al.*, 1996), we find that the cell activation parameter, which is the inverse of cell excitability, decreases during spiral wave progression (Figure 5). This result illustrates how we can identify key signalling properties of the cells from their population signalling patterns, at each time point during aggregation. Plotting N_0 from equation (4) against the wave period T provides a prediction of the *dispersion relation*, which quantifies how a decrease in wave period reduces the wave speed because cells do not fully reset between waves, causing them to activate slower. The *curvature relation* describes the relationship between radius and rate of circulation of the spiral tip:

$$\varepsilon = \frac{\omega}{\mathrm{D}\,\Omega(k, r_0)} \quad , \qquad \Omega = \frac{k(1 + 4kr_0 - \sqrt{1 + 8kr_0}\,)}{4\,r_0(1 + kr_0)}\,, \quad (5)$$

where r_0 is the radius of spiral tip circulation, which can measure form our data. In support of our approach, the curvature and eikonal relations produce similar values of the cell activation parameter at all time points. We use the curvature relation to predict the circulation radius of the spiral tip based on our spiral measurements.

Mathematical model (PDE)

To test whether the coupling of cell excitability to the external [cAMP] dynamics sufficiently describes spiral wave progression, we extended a mathematical model of cAMP spiral waves to simulate the time evolution of the external [cAMP] field over time. We adopt the model by Tyson et al. (Tyson and Murray, 1989), which is of the general form of continuum excitable media (equation (1)) with the dynamics of cAMP release (functions f and g in equation (1)) governed by the Martiel-Goldbeter model:

$$\tau\frac{\partial u}{\partial t} = \tau\,\varepsilon\,D\,\nabla^2 u + \frac{1}{\varepsilon}(\alpha_u f_+(u,v) - \beta_u u), \quad \tau\frac{\partial v}{\partial t} = g_+(u)(1-v) - g_-(u)v\,, \qquad (6)$$

$$f_+(u,v) = \frac{\lambda_1 + Y^2}{\lambda_2 + Y^2}\,, \qquad Y = \frac{u\,v}{1+u}\,, \qquad g_+ = \frac{L_1 + \kappa L_2 c u}{1 + cu}, \qquad g_- = \frac{1 + \kappa u}{1 + u}$$

where u and v (non-dimensional) is the spatial distribution of external [cAMP] (which can diffuse) and an internal inactivator (which cannot diffuse). We adopted the following non-dimensional parameter

values from Ref X, most of which were rounded to the nearest order of magnitude: $\alpha_u = 10^3, \beta_u = 10^2, \kappa = 10^1, L_1 = 10^1, L_2 = 10^{-1}, \lambda_1 = 10^{-4}, \lambda_2 = 0.5, c = 10^1$. Equation (6) is dimensionalised by the timescale $\tau = 0.075$ min and diffusion coefficient $D = 3 \times 10^4$ μm²/min. We note that solutions to this equation rapidly tend to an equilibrium state. Motivated by our finding that the cell excitability is coupled to the cAMP wave dynamics, we extended equation (6) by letting the cell activation variable, which we previously called the cell activation parameter (this inverse being a measure of cell excitability), to be a simple time-dependent function of the external [cAMP]:

$$\tau \frac{\partial \varepsilon}{\partial t} = \alpha_\varepsilon \, (\varepsilon_0 - \varepsilon) - \beta_\varepsilon \, u \, \varepsilon \, , \qquad (7)$$

Where $\alpha_\varepsilon = \frac{1}{50}, \beta_\varepsilon = \frac{35}{50}, \varepsilon_0 = 10$. Equation (7) states that the cell activation variable tends to a baseline value and decreases in response to external cAMP. The simulations were performed on a 4.5mmx4.5mm grid with 0.025mm spacing and 0.05min time step. The initial condition was the state where $u = 0, v = 0, \varepsilon = \frac{\varepsilon_0}{2}$, except for a rectangular region representing a broken wave, with $u = 10$ and $v = 0$ and to one side $u = 0$ and $v = 1$. To numerically solve equations (6) and (7) we used the implicit finite difference method for the diffusion term and the Runge-Kutta (Matlab ode45 function) method for the reaction terms. The Neumman boundary condition (no flux) was used.

Mathematical model (ABM)

A hybrid partial differential equation (PDE) agent-based model (ABM) was developed to study the interplay between cell motion, spiral wave dynamics and spatial patterning of cells around the spiral core. The 2D external [cAMP] field c was modelled by the following reaction-diffusion equation:

$$\partial_t c = D\nabla^2 c - \beta c + \sigma \sum_{i=1}^{N} H(A_i)\delta(\boldsymbol{x} - \boldsymbol{X}_i) \ ,$$

where β and σ are the rates of external cAMP decay and release from individual cells, D is the external cAMP diffusion coefficient, N is the number of cells, H is the Heaviside function, δ is the Dirac delta function, modelling the point source release of cAMP from cell i ($1 \leq i \leq N$), with position $\boldsymbol{X}_i$ and activation state A_i. We used the same parameter values as in Ref. (Vidal-Henriquez and Gholami, 2019). The following modified FitzHugh-Nagumo model was used to describe the excitable release of cAMP from each cell:

$$\tau \, \dot{A}_i = A_i - \frac{1}{3}A_i^3 - I_i + \alpha \, \log\left(1 + \frac{c_i}{\kappa}\right) \ , \ \ \tau \, \dot{I}_i = \epsilon(A_i - \gamma I_i + \mu) \ ,$$

where I_i is the inhibitor level of cell i, and the value of each parameter was the same as Ref. (Sgro *et al.*, 2015) with exception of the time scale τ which was adjusted to match experimental data. We tested several mathematical models of cell chemotaxis against the data for the velocity of individual

cells as a function of the external cAMP field. The external cAMP field was inferred in our experimental data by substituting the measured position and discretised activation state of each cell in the reaction-diffusion equation above, which provides a prediction for the external [cAMP] at the location of each cell $c_i = c_i(\boldsymbol{X}_i(t), t)$ and the spatial gradient $|c_i|$ (Figure 7–Video 2 and 7). The model that best fit the experimental data was a simple system of linear ordinary differential equations that encapsulate chemotactic memory:

$$\dot{\theta}_i = \alpha_m\, s_i\, |\nabla c_i|\, \sin(\theta_i^c - \theta_i)\ , \qquad \dot{v}_i = \beta_m\, s_i\, |\nabla c_i| - \gamma_m\, v_i\ , \quad \dot{s}_i = \sigma_m(1 - s_i) - \lambda_m\, c_i\, s_i\ ,$$

where θ_i and v_i are the direction and speed of cell movement and and s_i is the sensation variable to external cAMP as used in Ref. (Hofer, Sherratt and Maini, 1995). This variable causes cell chemotaxis to be sensitive to the external cAMP gradient at the front of the wave, but not the rear. Variable and θ_i^c is the direction of the external [cAMP] spatial gradient and model parameters α_m, β_m, γ_m, σ_m and λ_m were optimised using the Matlab function fminsearch to obtained the best fit experimental data. For the final cell movement model we also model size exclusion effects between cells, by including a cell-cell repulsion term. Model equations were solved numerically using Matlab. The external [cAMP] field was solved across a 50 grid points per mm length with the finite difference, implicit Euler method in time and central difference in space. Cell velocities and activation states were solved using the Matlab function ode45. Refer to Supplementary Material for the full model derivation and analysis. To initialize a spiral wave, we (i) disabled cell movement and let a vertical cAMP wave move from left to right across a periodic domain until it was equilibrated, (ii) then in the upper half of the domain, we set the external cAMP in the to zero and the inhibitor value to a high value (2.5) and finally (iii) set the boundary conditions to no-flux. See Supplementary Information for more detail.

References

Afonso, P. v. *et al.* (2012) 'LTB4 Is a Signal-Relay Molecule during Neutrophil Chemotaxis', *Developmental Cell*, 22(5). Available at: https://doi.org/10.1016/j.devcel.2012.02.003.

Agladze, K.I. and Krinsky, V.I. (1982) 'Multi-armed vortices in an active chemical medium', *Nature*, 296(5856). Available at: https://doi.org/10.1038/296424a0.

Aoki, K. *et al.* (2017) 'Propagating Wave of ERK Activation Orients Collective Cell Migration', *Developmental Cell*, 43(3). Available at: https://doi.org/10.1016/j.devcel.2017.10.016.

Cai, H. *et al.* (2014) 'Nucleocytoplasmic shuttling of a GATA transcription factor functions as a development timer', *Science*, 343(6177). Available at: https://doi.org/10.1126/science.1249531.

Chou, K.-T. *et al.* (2022) 'A segmentation clock patterns cellular differentiation in a bacterial biofilm', *Cell*, 185(1), pp. 145-157.e13. Available at: https://doi.org/10.1016/j.cell.2021.12.001.

Corrigan, A.M. and Chubb, J.R. (2014) 'Regulation of transcriptional bursting by a naturally oscillating signal', *Current Biology*, 24(2). Available at: https://doi.org/10.1016/j.cub.2013.12.011.

Crocker, J.C. and Grier, D.G. (1996) 'Methods of digital video microscopy for colloidal studies', *Journal of Colloid and Interface Science*, 179(1). Available at: https://doi.org/10.1006/jcis.1996.0217.

Deneke, V.E. and di Talia, S. (2018) 'Chemical waves in cell and developmental biology', *Journal of Cell Biology*. Available at: https://doi.org/10.1083/jcb.201701158.

Dieterle, P.B. *et al.* (2020) 'Dynamics of diffusive cell signaling relays', *eLife*, 9. Available at: https://doi.org/10.7554/eLife.61771.

Durston, A.J. (1973) 'Dictyostelium discoideum aggregation fields as excitable media', *Journal of Theoretical Biology*, 42(3). Available at: https://doi.org/10.1016/0022-5193(73)90242-7.

Durston, A.J. (2013) 'Dislocation is a developmental mechanism in dictyostelium and vertebrates', *Proceedings of the National Academy of Sciences of the United States of America*, 110(49). Available at: https://doi.org/10.1073/pnas.1300236110.

Ender, P. *et al.* (2022) 'Spatiotemporal control of ERK pulse frequency coordinates fate decisions during mammary acinar morphogenesis.', *Developmental cell* [Preprint]. Available at: https://doi.org/10.1016/j.devcel.2022.08.008.

Fisher, P.R., Merkl, R. and Gerisch, G. (1989) 'Quantitative analysis of cell motility and chemotaxis in Dictyostelium discoideum by using an image processing system and a novel chemotaxis chamber providing stationary chemical gradients.', *The Journal of cell biology*, 108(3). Available at: https://doi.org/10.1083/jcb.108.3.973.

Foerster, P., Muller, S.C. and Hess, B. (1990) 'Curvature and spiral geometry in aggregation patterns of Dictyostelium discoideum', *Development*, 109(1). Available at: https://doi.org/10.1242/dev.109.1.11.

Gelens, L., Anderson, G.A. and Ferrell, J.E. (2014) 'Spatial trigger waves: Positive feedback gets you a long way', *Molecular Biology of the Cell*. Available at: https://doi.org/10.1091/mbc.E14-08-1306.

Gregor, T. *et al.* (2010) 'The onset of collective behavior in social amoebae', *Science*, 328(5981). Available at: https://doi.org/10.1126/science.1183415.

Hashimura, H. *et al.* (2019) 'Collective cell migration of Dictyostelium without cAMP oscillations at multicellular stages', *Communications Biology*, 2(1). Available at: https://doi.org/10.1038/s42003-018-0273-6.

Hofer, T., Sherratt, J.A. and Maini, P.K. (1995) 'Dictydostelium discoideum: Cellular self-organization in an excitable biological medium', *Proceedings of the Royal Society B: Biological Sciences*, 259(1356). Available at: https://doi.org/10.1098/rspb.1995.0037.

Huang, X. *et al.* (2010) 'Spiral Wave Dynamics in Neocortex', *Neuron*, 68(5). Available at: https://doi.org/10.1016/j.neuron.2010.11.007.

Kamino, K. *et al.* (2017) 'Fold-change detection and scale invariance of cell-cell signaling in social amoeba', *Proceedings of the National Academy of Sciences of the United States of America*, 114(21). Available at: https://doi.org/10.1073/pnas.1702181114.

Lee, K.J., Cox, E.C. and Goldstein, R.E. (1996) 'Competing patterns of signaling activity in dictyostelium discoideum', *Physical Review Letters*, 76(7). Available at: https://doi.org/10.1103/PhysRevLett.76.1174.
Liu, L. *et al.* (2021) 'Nodal is a short-range morphogen with activity that spreads through a relay mechanism in human gastruloids', *bioRxiv* [Preprint].
Martiel, J.L. and Goldbeter, A. (1987) 'A Model Based on Receptor Desensitization for Cyclic AMP Signaling in Dictyostelium Cells', *Biophysical Journal*, 52(5). Available at: https://doi.org/10.1016/S0006-3495(87)83275-7.
Masaki, N. *et al.* (2013) 'Robustness of self-organizing chemoattractant field arising from precise pulse induction of its breakdown enzyme: a single-cell level analysis of PDE expression in Dictyostelium.', *Biophysical journal*, 104(5), pp. 1191–202. Available at: https://doi.org/10.1016/j.bpj.2013.01.023.
Miermont, A. *et al.* (2019) 'The fate of cells undergoing spontaneous DNA damage during development', *Development (Cambridge)*, 146(12). Available at: https://doi.org/10.1242/dev.174268.
Mirollo, R.E. and Strogatz, S.H. (1990) 'Synchronization of pulse-coupled biological oscillators', *SIAM Journal on Applied Mathematics*, 50(6). Available at: https://doi.org/10.1137/0150098.
Nakajima, A. *et al.* (2014) 'Rectified directional sensing in long-range cell migration', *Nature Communications*, 5. Available at: https://doi.org/10.1038/ncomms6367.
Nakajima, A. *et al.* (2016) 'The microfluidic lighthouse: An omnidirectional gradient generator', *Lab on a Chip*, 16(22). Available at: https://doi.org/10.1039/c6lc00898d.
Odaka, H. *et al.* (2014) 'Genetically-encoded yellow fluorescent cAMP indicator with an expanded dynamic range for dual-color imaging', *PLoS ONE*, 9(6). Available at: https://doi.org/10.1371/journal.pone.0100252.
van Oss, C. *et al.* (1996) 'Spatial pattern formation during aggregation of the slime mould Dictyostelium discoideum', *Journal of Theoretical Biology*, 181(3). Available at: https://doi.org/10.1006/jtbi.1996.0126.
de Palo, G., Yi, D. and Endres, R.G. (2017) 'A critical-like collective state leads to long-range cell communication in Dictyostelium discoideum aggregation', *PLoS Biology*, 15(4). Available at: https://doi.org/10.1371/journal.pbio.1002602.
Pandit, S. v. and Jalife, J. (2013) 'Rotors and the dynamics of cardiac fibrillation', *Circulation Research*. Available at: https://doi.org/10.1161/CIRCRESAHA.111.300158.
Paschke, P. *et al.* (2018) 'Rapid and efficient genetic engineering of both wild type and axenic strains of Dictyostelium discoideum', *PLoS ONE*, 13(5). Available at: https://doi.org/10.1371/journal.pone.0196809.
Pond, K.W. *et al.* (2022) 'Live-cell imaging in human colonic monolayers reveals ERK waves limit the stem cell compartment to maintain epithelial homeostasis.', *eLife*, 11. Available at: https://doi.org/10.7554/eLife.78837.
Sgro, A.E. *et al.* (2015) 'From intracellular signaling to population oscillations: bridging size- and time-scales in collective behavior', *Molecular Systems Biology*, 11(1). Available at: https://doi.org/10.15252/msb.20145352.
Siegert, F. and Weijer, C. (1989) 'Digital image processing of optical density wave propagation in Dictyostelium discoideum and analysis of the effects of caffeine and ammonia', *Journal of Cell Science*, 93(2). Available at: https://doi.org/10.1242/jcs.93.2.325.
Siegert, F. and Weijer, C.J. (1992) 'Three-dimensional scroll waves organize Dictyostelium slugs', *Proceedings of the National Academy of Sciences of the United States of America*, 89(14). Available at: https://doi.org/10.1073/pnas.89.14.6433.
Siegert, F. and Weijer, C.J. (1995) 'Spiral and concentric waves organize multicellular Dictyostelium mounds', *Current Biology*, 5(8). Available at: https://doi.org/10.1016/S0960-9822(95)00184-9.

Skoge, M. *et al.* (2014) 'Cellular memory in eukaryotic chemotaxis', *Proceedings of the National Academy of Sciences of the United States of America*, 111(40). Available at: https://doi.org/10.1073/pnas.1412197111.

Song, L. *et al.* (2006) 'Dictyostelium discoideum chemotaxis: Threshold for directed motion', *European Journal of Cell Biology*, 85(9–10). Available at: https://doi.org/10.1016/j.ejcb.2006.01.012.

Stierl, M. *et al.* (2011) 'Light modulation of cellular cAMP by a small bacterial photoactivated adenylyl cyclase, bPAC, of the soil bacterium Beggiatoa', *Journal of Biological Chemistry*, 286(2). Available at: https://doi.org/10.1074/jbc.M110.185496.

Tomchik, K.J. and Devreotes, P.N. (1981) 'Adenosine 3',5'-monophosphate waves in Dictyostelium discoideum: A demonstration by isotope dilution-fluorography', *Science*, 212(4493). Available at: https://doi.org/10.1126/science.6259734.

Totz, J.F. *et al.* (2018) 'Spiral wave chimera states in large populations of coupled chemical oscillators', *Nature Physics*, 14(3). Available at: https://doi.org/10.1038/s41567-017-0005-8.

Tunnacliffe, E., Corrigan, A.M. and Chubb, J.R. (2018) 'Promoter-mediated diversification of transcriptional bursting dynamics following gene duplication', *Proceedings of the National Academy of Sciences of the United States of America*, 115(33). Available at: https://doi.org/10.1073/pnas.1800943115.

Tyson, J.J. *et al.* (1989) 'Spiral waves of cyclic amp in a model of slime mold aggregation', *Physica D: Nonlinear Phenomena*, 34(1–2). Available at: https://doi.org/10.1016/0167-2789(89)90234-0.

Tyson, J.J. and Keener, J.P. (1988) 'Singular perturbation theory of traveling waves in excitable media (a review)', *Physica D: Nonlinear Phenomena*, 32(3). Available at: https://doi.org/10.1016/0167-2789(88)90062-0.

Tyson, J.J. and Murray, J.D. (1989) 'Cyclic AMP waves during aggregation of Dictyostelium amoebae', *Development*. Available at: https://doi.org/10.1242/dev.106.3.421.

Varnum, B., Edwards, K.B. and Soll, D.R. (1985) 'Dictyostelium amebae alter motility differently in response to increasing versus decreasing temporal gradients of cAMP', *Journal of Cell Biology*, 101(1). Available at: https://doi.org/10.1083/jcb.101.1.1.

Vidal-Henriquez, E. and Gholami, A. (2019) 'Spontaneous center formation in Dictyostelium discoideum', *Scientific Reports*, 9(1). Available at: https://doi.org/10.1038/s41598-019-40373-4.

Weijer, C.J. (2004) 'Dictyostelium morphogenesis', *Current Opinion in Genetics and Development*. Available at: https://doi.org/10.1016/j.gde.2004.06.006.

Wessels, D., Murray, J. and Soll, D.R. (1992) 'Behavior of Dictyostelium amoebae is regulated primarily by the temporal dynamic of the natural cAMP wave', *Cell Motility and the Cytoskeleton*, 23(2). Available at: https://doi.org/10.1002/cm.970230207.

Winfree, A.T. (1972) 'Spiral waves of chemical activity', *Science*, 175(4022). Available at: https://doi.org/10.1126/science.175.4022.634.

Winfree, A.T. (2001) *The geometry of biological time: Interdisciplinary applied mathematics*, *Springer*.

Supplementary Material: Mathematical Model (ABM)

In this section we give a detailed description of the computational model used to mimic and examine the collective dynamics of *Dictyostelium* cells.

General Model Set-up

We use a hybrid computational model in two space dimensions. Cells are modelled as discrete elements, while the external cAMP concentration ([cAMP]) is represented as a continuous function. Cells are labelled by index $i = 1, \dots, N$ where N is the total number of cells. Each cell has a number of properties (position, speed, internal signalling dynamics, etc.). Cells produce external cAMP, which diffuses and decays. Cells also sense external cAMP, which influences their internal dynamics and movement. The spatial domain is $\Omega = \left[-\frac{L}{2}, \frac{L}{2}\right]^2 \subset \mathbb{R}^2$ where $L > 0$ is the domain size. The external [cAMP] at position x and time t is denoted by $c(\boldsymbol{x}, t)$ for $t \geq 0$ and $\boldsymbol{x} \in \Omega$ and cells are positioned at $\boldsymbol{X}_i(t) \in \Omega$.

Internal Signalling Dynamics

Several models of internal cAMP dynamics have been suggested (Martiel and Goldbeter, 1987; Gregor *et al.*, 2010; Sgro *et al.*, 2015; Kamino *et al.*, 2017). We choose to work with the model used in Ref. (Sgro *et al.*, 2015) which has been shown to be able to reproduce a wider range of experimental observations than other models. The model is based on the famous FitzHugh-Nagumo model originally developed for spike generation in axons.

Let $A_i(t)$ and $I_i(t)$ represent activator and inhibitor dynamics of the i-th cell. Note that while they do not represent concentrations of specific molecules, we assume that the value of the activator determines cAMP release to the exterior of the cell. The dynamics are governed by:

$$\tau\, \dot{A}_i = A_i - \frac{1}{3} A_i^3 - I_i + \alpha\, \log\left(1 + \frac{c_i}{\kappa}\right), \quad \tau\, \dot{I}_i = \epsilon(A_i - \gamma I_i + \mu), \qquad (1)$$

where $c_i = c(\boldsymbol{X}_i(t), t)$ is the concentration of external cAMP experienced by the i-th cell. We use the parameters from (Sgro *et al.*, 2015) and fit the time scale parameter τ to match the experimentally measured spiking frequency (see Table 1).

External cAMP dynamics

External cAMP is secreted by active cells. We define active cells as having a positive activator value $A_i > 0$ (Sgro *et al.*, 2015). Once secreted, we assume external cAMP diffuses and decays. We note that other, more complicated dynamics of external cAMP have been used (e.g. active degradation by

cells (Hofer, Sherratt and Maini, 1995), however here we chose to omit such potential effects in the interest of simplicity. We use the following equation:

$$\partial_t c = D\nabla^2 c - \beta c + \sigma \sum_{i=1}^{N} H(A_i)\delta(\boldsymbol{x} - \boldsymbol{X}_i) \ , \quad (2)$$

where D is the diffusion constant, β the decay rate and σ the external cAMP secretion rate of active cells. H is the Heaviside function, i.e. only for $A_i > 0$ cells secrete cAMP, and δ denotes a smooth approximation of the Dirac delta function. For numerical efficiency we use the product of two one-dimensional bump functions, i.e. if $\boldsymbol{x} = (x, y)$, then $\delta(\boldsymbol{x}) = b(x)b(y)$ where $b(r) = \frac{1}{Z}\exp(-\frac{1}{1-\left(\frac{r}{d}\right)^2})$ for $r < d$and zero otherwise. The constant Z is a normalisation constant chosen such that δ has mass 1. The parameter d has units of space and can be interpreted as the size over which an activated cell secretes cAMP. Since we don't measure external cAMP explicitly, we don't specify the units of external cAMP, but just refer to the units as "conc". For parameters see Table 1.

Chemotaxis Model

Numerical and experimental results indicate that while the gradient of external cAMP plays a critical role in determining cell direction, whether cells are sensitive to the gradient and how this in turn affects their velocity remains largely unclear.

A data-driven approach was used to infer an accurate yet simple mathematical model of single-cell *Dictyostelium* chemotaxis in response to dynamics external [cAMP] fields. To achieve this, we first used equation (2) to predict the external [cAMP] field using the experimentally measured cell positions and internal cAMP states as inputs. Using the inferred [cAMP] field we generated the time series (2 hours, 5 second intervals) for the external [cAMP] magnitude and gradient for each cell (in addition to the cell signalling state and velocity) in the central 1mm x 1mm area of the experimental field of view (1.2mm x 1.2mm). We then systematically compared how well the predicted external [cAMP] field can explain measured cell movement under various chemotaxis model assumptions. We started with simple models such as:

$$\dot{\boldsymbol{X}}_i = \alpha \nabla c_i$$

Here $\boldsymbol{X}_i(t)$is the cell velocity and ∇c_i is the external [cAMP] gradient. The Matlab function fminsearch was used to identify parameter values that minimise the mean difference in the measured and predicted direction and magnitude of cell velocity for each cell track. We then identified the shortcoming of each model, and added model complexity. For example, from the equation above, we incorporated receptor desensitisation, yielding the same model as in Ref. (Hofer, Sherratt and Maini, 1995):

$$\dot{\boldsymbol{X}}_i = \alpha \nabla c_i \ , \quad \dot{s}_i = a\,(1 - s_i) - b\, c_i\, s_i$$

and s_i is the number of receptors on the surface and encapsulates receptor desensitisation. This process motivated the use of the development of the following chemotaxis model:

$$\dot{\theta}_i = \alpha_m\, s_i\, |\nabla c_i|\, \sin(\theta_i^c - \theta_i)\ ,\ \dot{v}_i = \beta_m\, s_i\, |\nabla c_i| - \gamma_m\, v_i\ ,\quad \dot{s}_i = \sigma_m(1 - s_i) - \lambda_m\, c_i\, s_i\ , \qquad (3)$$

where $0 \leq \theta_i < 2\pi$ and $v_i \geq 0$ are the direction and speed of cell movement and and $s_i \geq 0$ is the sensation variable to external cAMP as used in Ref. (Hofer, Sherratt and Maini, 1995). Variable $|\nabla c_i|$ and $0 \leq \theta_i^c < 2\pi$ are respectively the magnitude and direction of the external [cAMP] spatial gradient evaluated at $\boldsymbol{X}_i$. The parameters α_m, β_m, γ_m, σ_m and λ_m are determined during the model identification and fitting method described above (see Table 1). The first equation models the turning of the cell towards the local gradient of external cAMP. The turning speed depends on a cell's sensitivity and the size of the cAMP gradient. The second equation describes adaptation of the cell speed. It drives cell speed to be proportional to $s_i\, |\nabla c_i|$, i.e. higher sensitivity and larger local gradients will lead to faster speeds. Finally, the third equation models sensitivity: If a cell experiences a high concentration of external cAMP c_i, it will become de-sensitised and it takes some time to become sensitive again. The variable s_i provides “inertia” or “memory”, that makes cell chemotaxis to be dependent on the history of external [cAMP] dynamics. When comparing the model predictions to the data, this effect was crucial to ensure that cells move towards the wave source at the wave front while also neglecting the wave rear. Specifically, between waves the value of s_i recovers to a state where the cells are sensitive to the external cAMP gradient at the front of the wave, but subsequently s_i reduces to a state where the cells are insensitive to the external cAMP gradient at the rear of the wave.

For the final cell movement model, we also consider size exclusion effects between cells, by including a cell-cell repulsion term. This means θ_i and v_i are understood to mean the orientation and speed a cell would have if not in contact with other cells. We define as $d_{ij} = |\boldsymbol{X}_i - \boldsymbol{X}_j|$ the distance between the cell centres of the i-th and j-th cell. A cell's movement now follows:

$$\dot{\boldsymbol{X}}_i = v_i(\cos\theta_i\, , \sin\theta_i) + \rho_R \sum_{j \neq i, d_{ij} < d_R} \left(1 - \frac{d_{ij}}{d_R}\right) \frac{\boldsymbol{X}_i - \boldsymbol{X}_j}{d_{ij}}\, , \qquad (4)$$

i.e. cells move with speed v_i in direction θ_i in the absence of cell-cell repulsion. The second term describes a cell-cell repulsion with maximal repulsion magnitude ρ_R where only cells within a distance of d_R of each other exert a pushing force.

Initial and boundary conditions

We use no-flux boundary conditions for the external cAMP concentration, i.e. cAMP cannot leave the domain. Similarly cells cannot leave the domain. Since the dynamics cause a concentration of cells towards the spiral center, cells are being depleted from the very edge of the simulation domain and

hence we only considered the middle part of the simulation domain to represent the biological situation.

For all numerical experiments we initialise cell positions $\boldsymbol{X}_i$ and orientations θ_i using a uniform random distribution on Ω and $[0, 2\pi)$ respectively. Cell sensitivities s_i were initially set to 1 and cell speeds v_i to 0. The initial external cAMP concentration, activator and inhibitor values were initialised as shown in Supplementary Figure 1. The values shown in Supplementary Figure 1 were created by disabling cell movement and

1. Letting a vertical cAMP wave moving from left to right across a periodic domain until it is equilibrated,
2. Setting the external cAMP in the upper-half of the domain to zero and setting the inhibitor value in the upper half on the domain to a high value (we used 2.5) and
3. Setting the boundary conditions to no-flux and restarting the simulation.

Numerics

We solve equations (1)-(4) numerically using Matlab.

We discretise $c(\boldsymbol{x}, t)$on a regular rectangular spatial grid using 50 gridpoints per mm length. To solve equation (2) we use a finite difference, implicit Euler method in time (time step Δt), using a central difference in space (spatial step Δx) discretisation for the diffusion term. The source term is taken explicitly, i.e. evaluated at the current time step.

The internal cAMP dynamics (equation (1)) as well as dynamics of the chemotaxis related quantities (equation (3)) are solved on $[t, t + \Delta t]$ using the in-built Matlab solver ode45. Finally, equation (4) is solved using an explicit Euler method (time step Δt).

Symbol	Meaning	Value/unit	Reference
$c(\boldsymbol{x}, t)$	External [cAMP]	Conc	
$\boldsymbol{X}_i(t)$	Cell position	(mm, mm)	
$A_i(t)$	cAMP activator	a.u.	
$I_i(t)$	cAMP inhibitor	a.u.	
$\theta_i(t)$	Cell orientation	Radians	
$v_i(t)$	Cell speed	mm/min	
$s_i(t)$	Cell sensitivity	a.u., [0, 1]	
τ	Time scale of cAMP dynamics	0.167 min	Fitted
ε	Activator and inhibitor time scale	0.1	(Sgro *et al.*, 2015)
γ	ratio	0.5	(Sgro *et al.*, 2015)

μ	Inhibitor decay rate	1.2	(Sgro *et al.*, 2015)
α	Basal inhibitor production	0.058	(Sgro *et al.*, 2015)
κ	cAMP response magnitude cAMP response threshold	10^{-5} conc	(Sgro *et al.*, 2015)
D	External cAMP diffusion constant	2.4×10^{-2} mm^2 min^{-1}	(Hofer, Sherratt and Maini, 1995)
β	External cAMP degradation rate	5 min^{-1}	
σ	External cAMP secretion rate	10^3 conc mm^2 min^{-1}	Estimated
d	External cAMP secretion length scale	0.1 mm	
α_m	Maximal turning rate	3×10^{-6} mm min^{-1} conc^{-1}	Fitted
β_m	Speed model parameter 1	10^{-8} mm^2 min^{-2} conc^{-1}	Fitted
γ_m	Speed model parameter 2	0.6 min^{-1}	Fitted
σ_m	Re-sensitisation rate	150 min^{-1}	Fitted
λ_m	De-sensitisation rate	4×10^{-3} min^{-1} conc^{-1}	Fitted
ρ_R	Maximum repulsion strength	0.1 mm min^{-1}	Estimated
d_R	Cell radius	5×10^{-3} mm	Measured
L	Domain length	4 mm	
Δx	Spatial step	0.02 mm	
Δt	Temporal step	0.05 min	

Table 1 Model parameters.